Università degli Studi di Genova

Scuola politecnica

DICCA

Dipartimento di Ingegneria Civile, Chimica
e Ambientale

Master of science thesis in
Mechanical Engineering
Energy and Aeronautics

Drag reduction through fractal riblets

Author
Mattia Gribaudo

Supervisor
Prof. Alessandro Bottaro

Co-Supervisor
Dr. Edoardo Alinovi

October 2017

Università degli Studi di Genova
Scuola Politecnica
DICCA
Dipartimento di Ingegneria Civile, Chimica
e Ambientale

Tesi di Laurea in
Ingegneria Meccanica
Energia e Aeronautica

Riduzione della resistenza fluidodinamica mediante riblets frattali

Autore
Mattia Gribaudo

Relatore
Prof. Alessandro Bottaro

Correlatore
Dr. Edoardo Alinovi

Ottobre 2017

A Rita e Maria.

Abstract

Skin friction or viscous drag is currently considered the major barrier to the further optimization of the most aerodynamics and hydrodynamics bodies. One of the most appealing method to reduce the skin friction consists in texturing the body surface with micro-grooves aligned to the flow direction. Such a corrugations take the name of riblets, and, according to experiments, they are able to reduce the skin friction drag from 4% up to 10%.

The present work aim at evaluating the influence of the nanoscopic surface features in a turbulent boundary layer. The small geometric structure is taken under consideration by means of a particular riblet shape: the fractal riblet.

The investigation is subdivided in two parts, the microscopic and the macroscopic problem. In the first problem, the viscous flow near the grooved surface is concerned. Its solution allows to find out the longitudinal and the transverse protrusion heights, two fundamental quantities which describe the riblets effectiveness.

The macroscopic problem aims at quantifying the drag reduction induced by a flat surface coated with fractal riblets. The computations are performed through direct numerical simulations of a rectangular channel at moderate Reynolds number. In order to take under consideration the ribletted walls, the protrusion heights are used inside the Navier boundary conditions in both the stream-wise and span-wise directions.

The results reveal that the nanoscopic structure of the riblet has a positive influence on the riblet effectiveness, and that fractal riblets can enhance the skin friction drag reduction up to 2%.

Sommario

Ad oggi, la resistenza fluidodinamica viscosa rappresenta l'ostacolo maggiore all'ulteriore ottimizzazione dell'aerodinamica e dell'idrodinamica dei mezzi di trasporto. Una delle soluzioni di maggior interesse è l'utilizzo di superfici che presentano scanalature lungo la direzione del flusso, chiamate riblets e capaci di ridurre l'attrito viscoso in un range che va dal 4% al 10%.

Il presente lavoro di tesi si propone di valutare l'influenza delle strutture nanoscopiche sulla capacità dei riblet di ridurre l'attrito. Questo tipo di strutture sono prese in considerazione tramite lo studio di corrugazioni frattali.

Lo studio è suddiviso in due parti: il problema microscopico e quello macorscopico. Il primo prende in considerazione il flusso vicino alla parete, dove le forze viscose sono dominanti. La soluzione ottenuta permette di calcolare l'altezza di protrusione longitudinale e quella trasversale, che forniscono un'indicazione dell'efficacia dei riblets.

Il problema macroscopico viene risolto per determinare la resistenza fluidodinamica delle pareti con i riblet semplici e frattali. A tal fine, viene risolto numericamente il flusso in un canale, a basso numero di reynolds e consideranto tutte le scale della turbolenza (DNS). Inoltre, per rappresentare i riblet vengono utilizzate delle condizioni al contorno di Navier, in cui come lunghezze di slip vengono considerate le altezze di protrusione.

I risultati mostrano che le nanostrutture superficiali influiscono fortemente sull'efficacia dei riblet, inoltre viene motrato come i riblet frattali sono in grado di aumentare la riduzione di attrito anche del 2%.

Ringraziamenti

Desidero ringraziare il Professor Alessandro Bottaro per avermi dato l'occasione di lavorare a questa tesi e per avermi offerto molte opportunità per il futuro.

Ringrazio il mio correlatore, l'Ingegner Edoardo Alinovi. E' sempre stato disponibile e mi ha dato consigli utili di cui farò tesoro, grazie.

Ringrazio tutti i miei amici, che mi sono stati vicini e sono riusciti a rallegrare le giornate peggiori.

Ringrazio soprattuttto Clelia, che è sempre stata al mio fianco, mi ha confortato nei periodi difficili, ed è riuscita a farmi vedere il lato positivo delle cose anche quando io non riuscivo a trovarlo.

Infine, un ringraziamento speciale va ai miei genitori Saura e Seba, che mi sono stati vicini nei momenti difficili di questi anni.

Contents

Chapter 1

Introduction

1.1 Drag reduction

Transport is the movement of people, animals and goods from one location to another, and it is important because it enables trade between people, which is essential for the development of civilizations. Unfortunately performing its fundamental role, transportation produces a lot of air pollution, it impoverishes local air quality, causes acidification and it is a major emitter of CO_2. The last report of the International Energy Agency and the Internationl Union of Railways point out that the $23,1\%$ of the CO_2 world emission in 2012 was due to the whole sector of transportation (Zambini [28]). Although the technologies employed in this sector grow up exponentially, the negative effects on the ambient still increase; for example, in 2014 the whole emission of the transportation sector in the European Union increase of 20 % with respect to the 1990. For the aforementioned and even economical reasons, the fuel consumption reductions is pursuited from years by all the companies involved in this sector. The thrust in this way has brought a lot of innovative solutions, upon to the development of the electric car, that certainly will be the future of transportation. However, there are a lot of other mechanisms that allow to obtain a reduction of the fuel consumption, and among these it is possible to find the viscous drag reduction.

Skin friction or viscous drag is currently considered the major barrier to the further optimization of most aerodynamic and hydrodynamic bodies. For various reasons, several classes of transport, notably automobiles, trucks, and helicopters, are still impacted by pressure drag and therefore these devices would not benefit materially from viscous drag reduction at the present time, since viscous drag is a small portion of their overall drag budget. Instead, the skin friction reduction is of interest for such applications as: high-speed aircraft, aerospace planes (order of 30-40 % skin-friction drag), transport aircraft, ships operated at low Froude number (order of 50 % skin-friction drag), most underwater bodies (70 % or greater skin-friction drag) (Bushnell [8]).
In the quest for drag reduction three methods seem to be the major contenders today (Luchini et al.[20]):

- Delaying the separation of the boundary layer by triggering an early transition to turbulent flow.

- Affecting the boundary layer by injection or suction of fluid.
- Modifying the viscosity of the fluid in the boundary layer by injection of a suitable different fluid or by changing its temperature.
- Texturing the wall with micro-grooves (with a dimension of about 100 μm) aligned along the main flow direction. Such a grooves take the name of riblets.

The first of these methods is technologically the most advanced, and used for a long time in airplane wings in at least some form; the second has been proposed mainly for internal flows, such as the transportation of very viscous fluids in long pipelines (Preziosi et al. [16]). Its application to external flows being considered too expansive. The fourth method, is very appealing because of its completely passive nature, but its mechanism of operation is not well understood, and in fact one may even wonder, a priori, why it should reduce drag at all. Nevertheless, the observation that such corrugations occur naturally in shark skin (Burdak [3]; Chernyshov et al. [4]) triggered the interest of researcher on the riblets. During the 80s it was experimentally shown (Bechert et al. [26]; Sawyer [23]; Choi [5]; McLean et al. [17]) that a reduction of 4-7 % compared to the drag of a smooth surface can indeed be achieved in turbulent flows. The percent of reduction seems to be small, but, for example, even viscous drag reductions as small as 10 % on the fuselage alone are significant when it is realized that these small reductions translate into a 350 million per year of fuel savings for the airlines companies (Walsh et al. [25]). The present work is focused on the drag reduction through a particular shape of riblets.

1.2 The riblets

In 1972 the NASA Langley Research Center begun a new skin-friction program in order to reduce the aircraft fuel consumption. After a lot of studies, in 1976, Dr. L. R. Ash had the idea that small flow-aligned fences might modify the near-wall structure of the turbulent boundary layer, thus reducing the skin-friction. The small fences were called "riblets", and a small research study was initiated at NASA Langley Resech Center (Bushnell [8]).

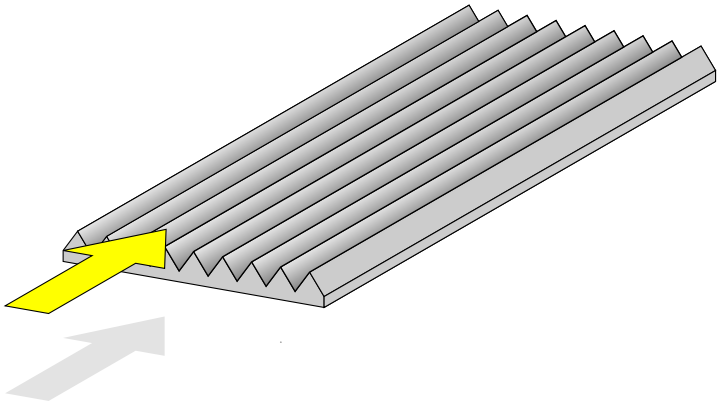

Figure 1.1: A model of a triangular riblet surface; the yellow arrow indicates the flow direction.

The idea that a longitudinally grooved surface could reduce the turbulent skin friction drag arises from a lot of experimental studies. Among these, the measurement of Klebanoff [15] which indicate that over 50 % of the turbulence energy is generated within the 5 % of the boundary layer, and the study of Kennedy et al. [14], that shows that turbulent shear stress is reduced by 40-45 % in the corners of a square duct.

Another important field of research that increase the interest in riblets surfaces, was the study of the shark skin. The interest of engineers in such a matter appared because the Reynolds number of fast sharks is comparatively high ($Re \sim 10^6 - 10^7$, calculated with the body length), and potential drag reducing mechanisms derived from shark skin are of technological interest (Bechert [26]). Moreover, there are some peculiarities with sharks. They are the oldest fish in terms of their evolutionary history; the ancestors of present day sharks already existed 350 million years ago and some families of living sharks have already existed since 190 million years. Thus, there has been a

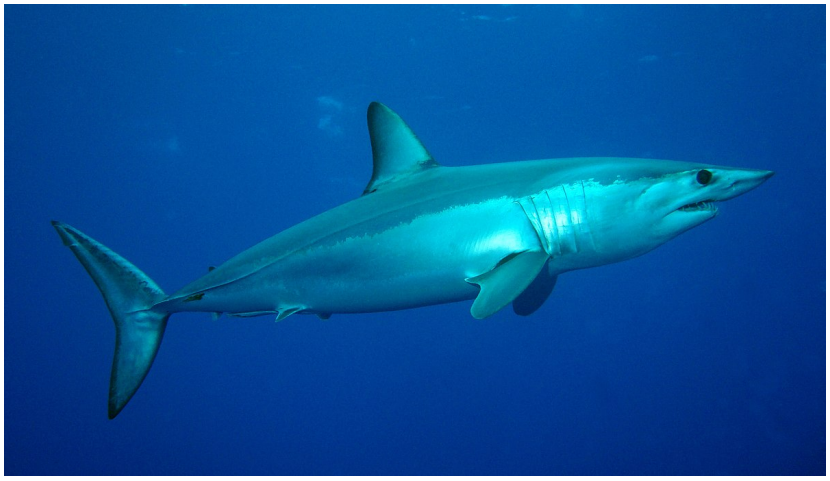

Figure 1.2: The Isurus Oxyrinchus, even called Mako, is one of the fastest shark on the planet. It can reach a maximum speed of 70 km/h.

comparatively long time for optimal adaption during their evolution. This optimization is also shown by other features related to swimming, like, e.g., the operation and the shape of the fins. In addition, because of their particular mode of intake of oxygen through their gills, which works only in forward motion, they move constantly, day and night, furthermore, the burst speed of off-shore predatory sharks (figure 1.2) is comparatively high, it is believed to be about 10 - 20 m/s. The relation between the ridge structure of shark scales of fast sharks and the drag reducing mechanism of riblets had been recognized by Reif and Dinkelacker [21]. Reif compiled information on shark scales for more than 40 species and from different growth stages, and the scales were taken from different parts of the shark bodies. With that material he could establish a correlation between ridge structure and velocity of different species. The results of this classification reveal that all fast off-shore sharks have scales with fine ridges (spacing 35-105 μm) shown in figure 1.3, whereas reef sharks have a similar scale structure but slightly wider ridge spacing. In contrast to that, slow sharks have completely different and largely varying scale patterns which may be interpreted as devices for protection against abrasion, parasites and predators. Therefore, in the spirit of biomimetics, a lot of "artificial shark-skin" have been built and tested. All the experimental measurement confirm that such a surface can reduce the skin-friction from 4 % up to 10 % depending on the surface. Other technique can be used to reduce the skin friction, however the grooved surfaces are the most appealing because of the following features:

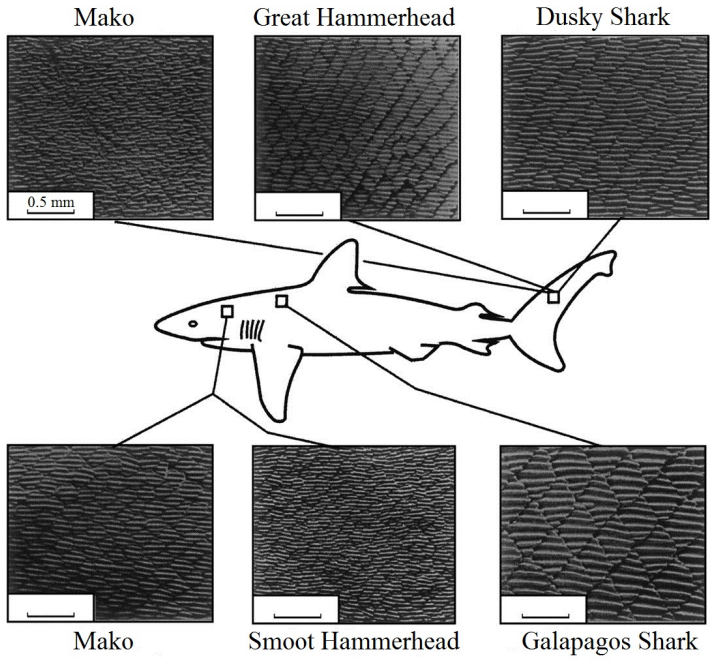

Figure 1.3: Different sharks have different kind of skin, but the faster sharks have all the same microscopic ridges.

- they are a passive drag-reduction technique (requires no additional energy).
- Their effectiveness is relatively unaffected by misalignment with the direction of the ow (Walsh et al. [25]; Choi et al. [5]) or by compressibility effects (McLean et al. [17])
- They are insensitive to the longitudinal pressure gradient (Baron et al. [1])

Although the effectiveness of the riblets is confirmed by experimental data, its mechanism of operation was not well understood.

When a turbulent flow develops on a ribletted surface, the lower part (valleys) of the small micro-grooves lie into the viscous sublayer, whereas the upper part (tips) protrude into the buffer layer. Such a confguration is advantageous for two principal reasons. First of all the sharp peaks damp the turbulence level, in fact they interact with the vortical structures (that take place in the buffer layer) and reduce the cross-flow. Moreover, the high velocity zones generated by the strem-wise vortex do not reach the riblet valleys, and this produces a low shear stress. Recent numerical simulation by (Douglas et al. [9]) confirm the aforementioned mechanism.

The foregoing argument is intuitively convincing, but it is only qualitative and it

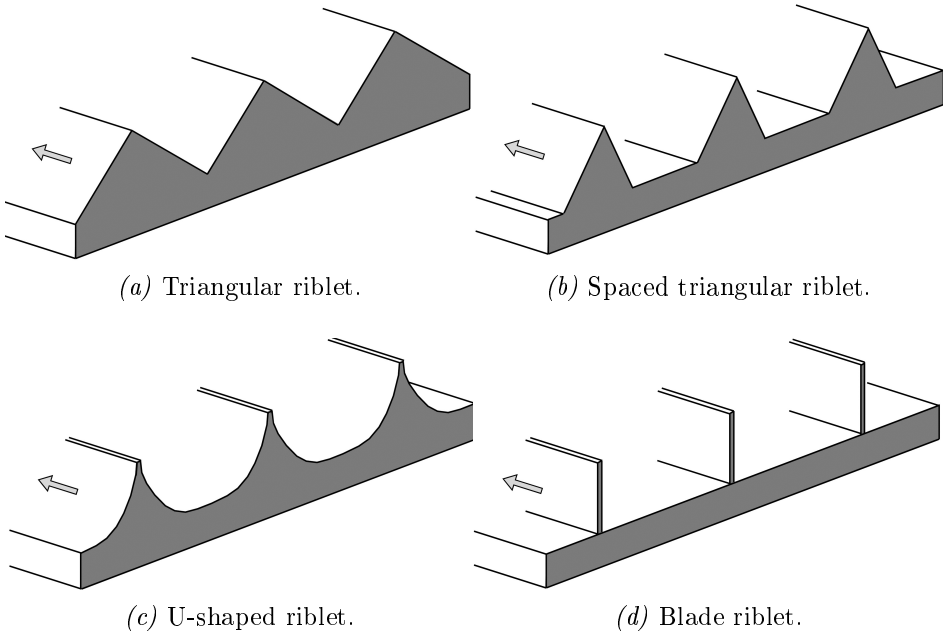

(a) Triangular riblet. *(b)* Spaced triangular riblet.

(c) U-shaped riblet. *(d)* Blade riblet.

Figure 1.4: Four kind of riblets shape.

can't be used to carry out a theory that allow to obtain the optimal shape of the riblets. Therefore, many variation in the basic riblet geometry have been testes in attempts to obtain an higher drag reduction; the most significant geometries are shown in figure 1.4: the v-groove riblets (sawtooth riblets) with various aspect ratios, the u-groove riblets (scalloped riblets), a spaced groove riblet, and rectangular riblets (blade riblets). However this is not an easy achievement, since the riblets give a small drag reduction (on the order of 6-8 %), therefore, the measurements require high accuracy. It is even more difficult to observe changes in drag reduction due to variations in geometry, since the changes in drag may be within the scatter of the measurements. In addition, the riblet performance can be quite sensitive to the quality of the machined surface: poor quality may result in rounding at the peaks, riblet aspect ratio varying across the surface, etc. Eventually, the machines resolution does not allow a perfect reproduction of the wanted riblet shape. All these problems may have an unknown influence on the performances.

Although the difficulties, a general trend of the drag reduction depending on the riblets spacing has been achieved. Figure 1.5 shows a typical drag reduction ($DR = -\Delta\tau_0/\tau_0$) curve as a function of the spacing (s^+), in which different drag regimes can be defined. In the viscous regime, formally $s^+ << 5$ but in practice $s^+ < 10 - 15$

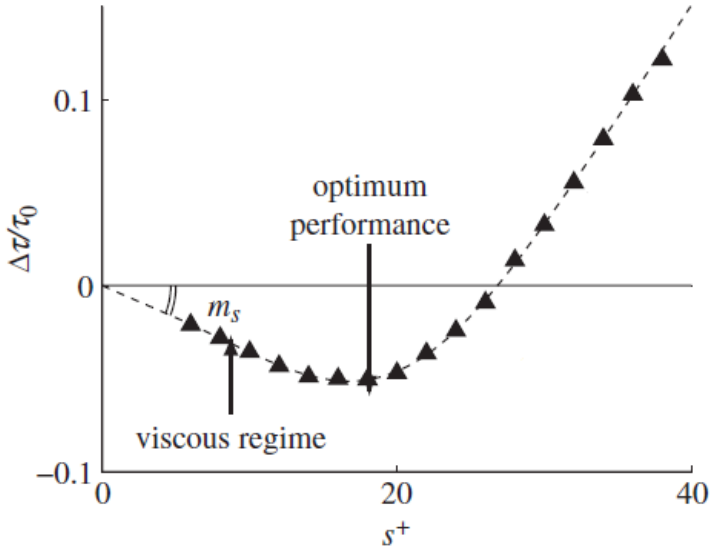

Figure 1.5: Definition of the drag-reduction regimes observed over triangular riblets with 60° tip angle, as a function of the peak-to-peak distance s^+.

, the contribution of the nonlinear terms to the flow within and in the immediate neighbourhood of the riblet grooves is negligible and, the drag reduction is proportional to s^+. The viscous regime breaks down near $s^+ = s^+_{opt}$, the optimum spacing for which drag reduction is maximum, and, eventually, the reduction becomes a drag increase, adopting a typical k-roughness behaviour. When riblet are too small the tips cannot well interact with the buffer layer and they cannot damp the secondary flow. However, if they are too large, the stream-wise vortex fall inside the riblet cavity and generate an high skin friction.

The numerical approach also presents some problems, in fact the small dimension of the grooves requires an extremely fine and complex grid. Therefore the time for the simulation may become very long.

1.3 The fractal geometries

In this section we leave momentarily the riblet topic in order to explain a particular geometry shape: the fractal. The reason will be clear in the next section, where this work purpose are explained.

The study of fractals is a very wide field, therefore this section aims to explain only the principal concepts, in order to understand why such a shape is taken under consideration. It is possible to get a rough idea of fractals, giving the following definition: a fractal is a geometric figure which exhibit similar patterns at increasingly small scales. In other words, magnifying such a object, one can always identify the same shape. This particular feature take the name of self-similarity, and can be employed to built a fractal object. Before proceeding with an example, it is worth to empathize that fractals exist only in a mathematical concept, in fact, fractals repeat itself at infinitely small length scale, generating an infinite long curve, that can enclose a finite area.

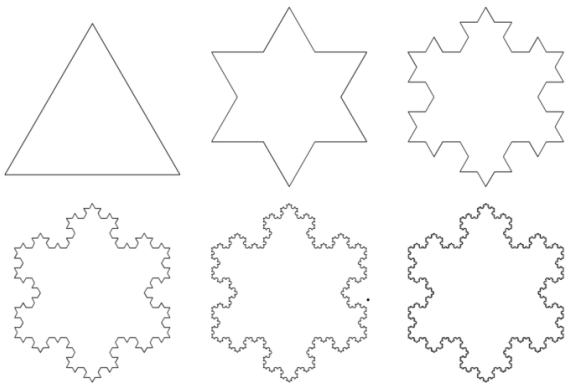

Figure 1.6: Original mold and five iterations of the Koch snowflake.

A quite famous fractal, the Koch curve shown in figure 1.6, can be constructed by starting with an equilateral triangle, then recursively altering each line segment as follows:

1. Divide the line segment into three segments of equal length.
2. Draw an equilateral triangle that has the middle segment from step 1 as its base and points outward.
3. Remove the line segment that is the base of the triangle from step 2.

We will use the these steps to construct fractal riblets.

1.4 Aim of the work

1.4.1 Case of study

This work aim at numerically studying the particular shape of riblet show in figure 1.7b that, until now, has not been taken under consideration: the fractal riblet.

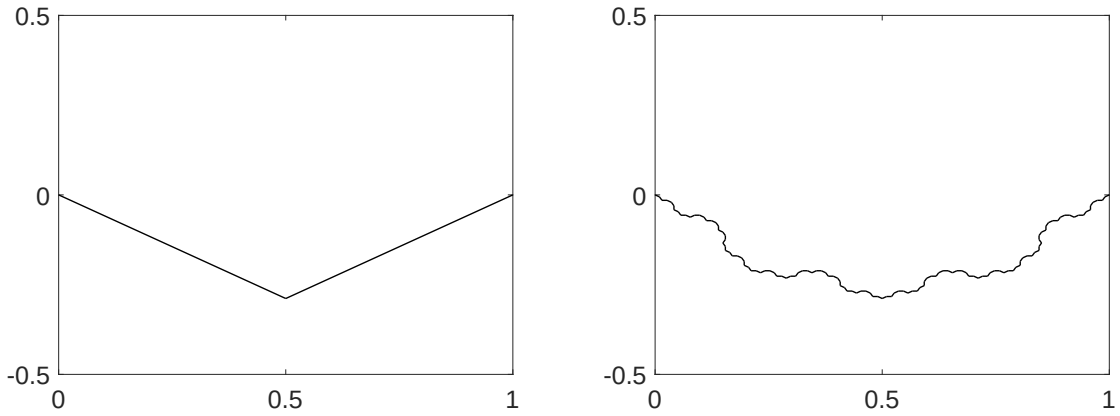

(a) Classical triangular riblet. *(b)* Fractal riblet.

Figure 1.7: Span-wise section of the classical triangular riblet shape and the fractal riblet, subject of this work.

This particular shape is carried out from the common triangular riblet through the application of the same steps presented in section 1.3, that have been used to built the Koch snowflake.

At this point, it is very important to stand out the reasons that bring us to choose such a geometry. In 1975, the mathematician Benoît Mandelbrot invented the name "fractal", and used it to extend the theoretical concept to the geometric patterns in nature, where it is possible to find a lot of self-similar shapes. Since then, fractals spreading throughout the science and became useful in a lot of fields of study. Thanks to the strong connection with all natural shapes, and according with others works [7], fractal are herein used to simulate the micro and nanoscopic structure of the riblet surface. The present study is based on the idea that the real surface is one of the key parameter to well reproduce the riblet effect. The aforementioned consideration is confirmed by the Baron et al. [1], which compares the drag reduction results between the ideal and the real riblet geometry.

Over the shape sketched in figure 1.7, we shall study others shapes, in order to have a comparison of results. All the geometry involved in this study are presented in section 2.7. In the next section we shall explain how the study of the fractal riblet is performed.

1.4.2 Description of the work

The study herein performed aim at carrying out the skin friction over a grooved fractal surface through the computational fluid dynamics (CFD). To do so we have decided to takle the problem in two parts: the microscopic and macroscopic problems.

The microscopic problem deals with the computation of the flow inside the boundary layer, very near the wall. In this region the momentum equation can be simplified in the Stokes equation and two fundamental quantities, the protrusion heights, can be determined. Afterwards, the computed protrusion heights are used as boundary condition for the marcoscopic problem, which allow to carry out the skin friction drag on the riblet plates taken under consideration.

Chapter 2

Microscopic problem

2.1 Viscous sublayer

The effect of drag reduction generated by the riblet surfaces has been discovered in the seventies, however the physical reasons that explain this phenomenon have been unknown for years. The route to a deeper understanding of the effects of grooved surfaces has been opened by Bechert's observation that the typical size of corrugations which appear to be experimentally effective is of the same order of magnitude as the height of the viscous sublayer of the turbulent stream [20]. In this work we consider a fully developed turbulent boundary layer (figure 2.1). It has a fundamental role in the present work, therefore we give a briefly description of it. To do so the dimensionless distance from the wall is introduces

$$y^+ = \frac{y}{\nu}\sqrt{\frac{\tau_w}{\rho_w}}, \tag{2.1}$$

thereby, the turbulent flow near a flat wall can be divided into four regions:

- The viscous sublayer ($0 \leq y^+ < 5$) : thin layer near the wall where the velocity is linear with the distance from the wall (if scaled properly); in this region the viscous effects are dominant.

- Buffer layer ($5 \leq y^+ < 30$): in this region the flow begins the transition to the turbulence and the viscous effects are of the same order of the convective one. The velocity profile is no longer linear.

- The Log-law region ($30 \leq y^+ < 500$): after the buffer region the transition is complete, the flow is fully turbulent and the average flow velocity is related to the logarithm of the distance to the wall. This is known as the log-law region and the convective effect are dominant on the viscous.

It is interesting to note that riblet are about $10 - 15$ unit wall, so the valleys stay in the viscous sulayer and tips in the buffer. We are interested to the layer just adjacent to the wall, the viscous sublayer. Whereas the main part of a turbulent boundary layer exhibits chaotic fluid motion, the viscous sublayer shows quite regular longitudinal vortex, which play a fundamental role in the momentum exchange and the turbulence generation. These regular patterns lead to the generation of the so called low-speed

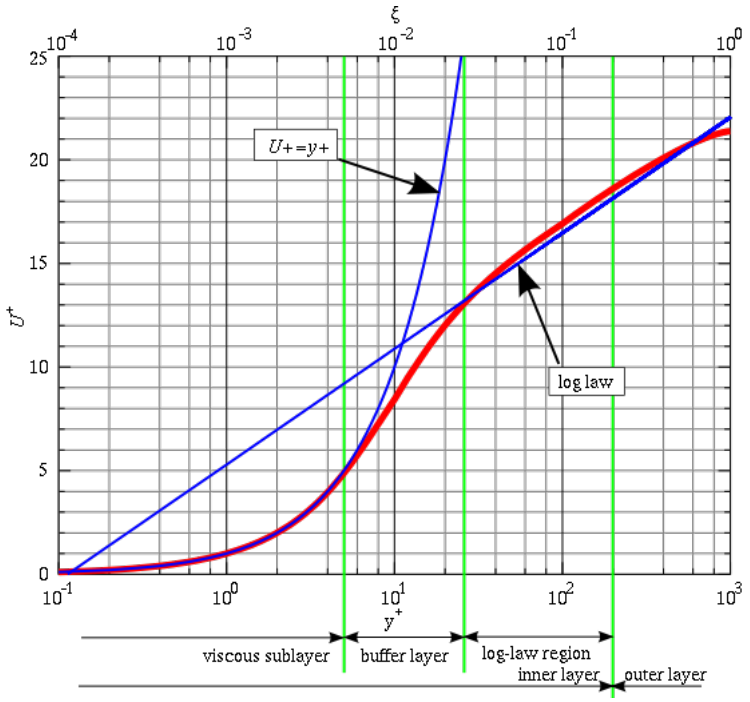

Figure 2.1: Structure of the turbulent boundary layer.

streaks, that will burst in the upper zones of the boundary layer and will promote turbulence.

The riblet are capable to obstacle the cross flow that generate such a structures, thereby they can hamper the turbulence production and increase the viscous sublayer thickness, as demonstrated by Hooshmand [10].

2.2 Mathemetical formulation

2.2.1 Stokes equation

In this section we present the passages that lead us to the governing equation of the flow in the viscous sublayer.

First of all we write the well known Navier-Stokes equations under the following hypothesis : Newtonian fluid, incompressible fluid and isothermal flow. Thanks to these assumption Navier-Stokes equations can be expressed in the following form:

$$\begin{cases} \nabla \cdot \mathbf{u} = 0 \\ \\ \rho \left[\dfrac{\partial \mathbf{u}}{\partial t} + (\mathbf{u} \cdot \nabla)\, \mathbf{u} \right] = -\nabla p + \mu \nabla^2 \mathbf{u}. \end{cases} \tag{2.2}$$

However, we focus the attention on the viscous sublayer, therefore, further simplifications are possible. Into such a region, the forces due to the viscosity of the fluid control the flow, and the inertial forces become negligible. In order to exploit this fact and simplify the equations, it is convenient to assess the importance of the various terms in the equation of motion. To achieve this goal, it is necessary to re-write the former equations 2.2 in the dimensionless form.

First of all we need to choose the characteristic dimension that allow us to yields all variables in dimensionless form; choosing L for the length scale, U for the velocity and T for the time, it is possible to introduce dimensionless variables and operators denoted by an hat, and defined as

$$\hat{\mathbf{u}} \equiv \frac{\mathbf{u}}{U}, \qquad \hat{\mathbf{x}} \equiv \frac{\mathbf{x}}{L}, \qquad \hat{\nabla} \equiv L\, \nabla, \qquad \hat{t} \equiv \frac{t}{T}, \qquad \hat{p} \equiv \frac{p\, L}{\mu\, U}. \tag{2.3}$$

Solving equations 2.3 for the physical variables in terms of the dimensionless ones and substituting into the equation of motion 2.2 results

$$\rho f U \frac{\partial \hat{\mathbf{u}}}{\partial \hat{t}} + \frac{\rho U^2}{L} \left(\hat{\mathbf{u}} \cdot \hat{\nabla} \right) \hat{\mathbf{u}} = -\frac{\mu U}{L^2} \hat{\nabla} \hat{p} + \frac{\mu U}{L^2} \hat{\nabla}^2 \hat{\mathbf{u}}. \tag{2.4}$$

Eventually multiplying for $L/\rho U^2$ the equation take the form

$$St\,\frac{\partial \hat{\mathbf{u}}}{\partial \hat{t}} + \left(\hat{\mathbf{u}} \cdot \hat{\nabla}\right) \hat{\mathbf{u}} = -\frac{1}{Re}\hat{\nabla}\hat{P} + \frac{1}{Re}\hat{\nabla}^2\hat{\mathbf{u}}, \tag{2.5}$$

where

$$St = f\frac{L}{U}, \qquad Re = \frac{\rho U L}{\mu}. \tag{2.6}$$

St is called Strouhal number and represent the unsteady effect due to the turbulent fluctuations, and Re is the Reynolds number, whose physical interpretation is the ratio of the inertial forces and the viscous ones. Thanks to this form of the equation, is now possible to evaluate the weight of each term.

Bechert et al. [27] conclude, also on the basis of experimental measurements by other authors, that the frequencies typically encountered in turbulent flow are low enough for the viscous sublayer to be treated as quasi-steady. Therefore, we suppose that $St \sim 0$ and we neglect the unsteady term.

The most important hypothesis, which is the heart of this study, concern the reynolds number. As explained in section 2.1 in the viscous sublayer the viscous forces are the most important ones, then it is possible to argue that $Re \sim 0$ or $1/Re \to \infty$. This bring to a very strong simplification: convective term is negligible respect to the diffusion and pressure term leading to

$$\hat{\nabla}\hat{P} = \hat{\nabla}^2\hat{\mathbf{u}}. \tag{2.7}$$

The relation 2.7, called Stokes equation, is the governing equation for all the creeping flow, in which the viscous forces are dominant. From now on, the hat over the dimensionless quantities is dropped for brevity, and the variables must be considered dimensionless.

2.2.2 Decoupling of the Stokes equation

We wish to study the Stokes flow of a viscous fluid alongside an infinite corrugated wall in the presence of a given shear, or velocity gradient, in the region far from the wall. For the sake of simplicity, we shall assume the wall surface to be translation-invariant

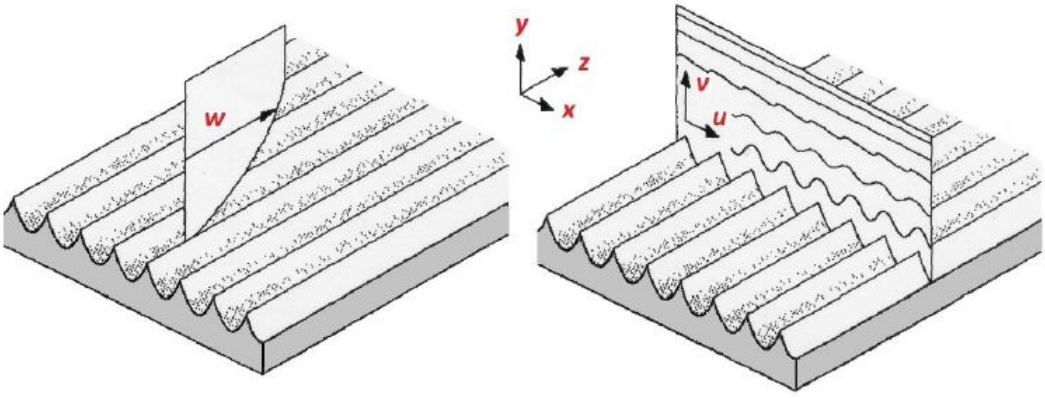

Figure 2.2: Wall texture and the reference coordinates.

in the z-direction, and periodic along the x-direction. The direction normal to these will be the y-axis as shown in figure 2.2. The geometric wall invariance along the z-axis suggest that physical quantities are too in the same direction. Under the assumption above, the equations 2.7 can be further simplified setting to zero all the derivatives in z

$$\begin{bmatrix} \frac{\partial P}{\partial x} \\ \\ \frac{\partial P}{\partial y} \\ \\ \cancel{\frac{\partial P}{\partial z}} \end{bmatrix} = \mu \begin{bmatrix} \frac{\partial^2 u}{\partial x^2} + \frac{\partial^2 u}{\partial y^2} + \cancel{\frac{\partial^2 u}{\partial z^2}} \\ \\ \frac{\partial^2 v}{\partial x^2} + \frac{\partial^2 v}{\partial y^2} + \cancel{\frac{\partial^2 v}{\partial z^2}} \\ \\ \frac{\partial^2 w}{\partial x^2} + \frac{\partial^2 w}{\partial y^2} + \cancel{\frac{\partial^2 w}{\partial z^2}} \end{bmatrix} \tag{2.8}$$

It is easy to observe that the problem become two dimensional, furthermore, the equation for w decouples from the system and it is just the Laplace equation. Therefore, the periodicity allows us to recast an initially 3D problem governed by the Stokes equation in two decoupled differential problems:

1. The longitudinal problem for the unknown velocity w

$$\begin{cases} \nabla^2 w = 0 \\ w(x, y_0) = 0 \\ w_y(x, \infty) = 1 \end{cases} \tag{2.9}$$

where y_0 is the periodic function that represent the profile of the wall in the plane

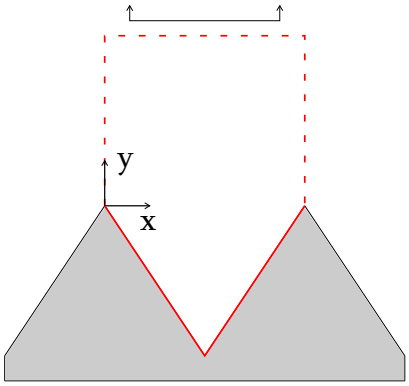

Figure 2.3: Domain contour (red line). The arrows on the upper part of the domain indicate that it must be considered far from the riblet wall.

(x,y).

2. The transverse problem for the unknowns u, v and P

$$\begin{cases} \nabla p = \nabla^2 \mathbf{u}, \mathbf{u} = (u, v) \\ \mathbf{u}(x, y_0) = (0, 0) \\ u_y(x, \infty) = 1 \end{cases} \tag{2.10}$$

These differential problems have been solved inside the domain shown in figure 2.3. The no slip boundary condition has been used at the wall, and a constant shear has been imposed far from the cavity.

2.3 Protrusion heights

It is important to define the concept of protrusion heights because we will use them as boundaries conditions for the macroscopic problem. We can define one protrusion height for each problem defined in section 2.2.2: the protrusion height associated with the parallel problem will be called parallel protrusion height, and that associated with the transverse problem will be called perpendicular protrusion height.

Now, let us proceed with the mathematical definition of the parallel protrusion height following the Luchini's passages [20]. Since w is periodic along x-axis, we can express it using the Fourier series

$$w = \sum_{n=-\infty}^{+\infty} W_n e^{inx}, \tag{2.11}$$

where

$$\begin{cases} W_n = a_n e^{-|n|y} + b_n e^{|n|y}, n \neq 0 \\ W_n = a_0 + b_0 y, n = 0. \end{cases} \tag{2.12}$$

The condition that $w_y = 1$ for $y \to +\infty$ fixes all b-coefficients as $b_0 = 1$ and $b_n = 0$ for $n \neq 0$, and leaves the a-coefficients to be determined by the condition at the wall surface. Since all the coefficients of the series 2.11 but W_0 vanish exponentially at infinity, the solution obtained will approach the linear behaviour $w \sim a_0 + y$, and thus it imitates the linear velocity profile produced by a plane wall located at $y = -a_0$. Parallel protrusion height is defined as $h_{||} = a_0$, and therefore it represents the distance of the aforementioned virtual plane wall from the y-axis origin (which is located on the riblet tips). This quantitiey have been first derived by Bechert et al. [27], that defined it as the apparent origin of the velocity profile on a grooved surface. Luchini shows that a similar protrusion height may be defined for the cross-flow as well, therefore it is even possible to write

$$w \sim h_{||} + y \tag{2.13}$$

$$u \sim h_{\perp} + y \tag{2.14}$$

being $h_{\perp}$ the perpendicular protrusion height, conceptually defined as the parallel one. They can be used to represent the influence of the riblets on the viscous sublayer. In

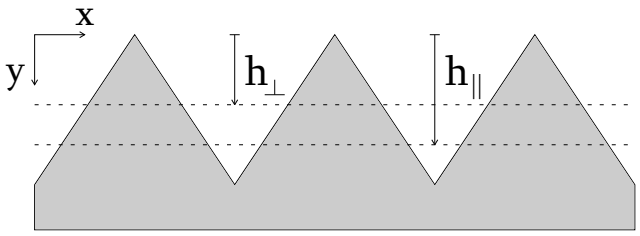

Figure 2.4: Cross-section of a riblet plates and protrusion heights.

figure 2.4 is shown the virtual plane wall which create the linear velocity profile.

It is important to note that the value of both parallel and perpendicular protrusion height depends on the origin f the coordinate system, hence we define a new quantity which does not depends on it

$$\Delta h = h_{||} - h_{\perp}. \tag{2.15}$$

The difference between the two protrusion heights (Δh) has been related to the effectiveness of riblets (Luchini et al. [20]). An high value of it imply an efficient riblet, hence an high drag reduction (DR). On the contrary, a low value of Δh is associated to lower drag reduction. This theory cannot reveals the drag reduction amount, but it can be used for a qualitative analysis. In the present work the relation between the drag reduction and the protrusion height difference is used to qualitatively analyze the fractal riblet effectiveness, moreover in the last chapter, a way to quantitatively relate Δh and DR is shown.

2.4 Boundary integral method

Over the last 30 years, a very popular method for solving partial differential equations has developed and matured. This elegant approach is the *Boundary Integral Method* (BIM) and it can be applied in many areas of the engineering and science, including fluid mechanics, acoustics, electromagnetics and fracture mechanics. The method aim at transforming a differential equation in an integral equation, called *Boundary Integral Equation* (BIE), which relate the unknown function into the domain to only the value on the boundary values. We now derive the boundary integral equation for the Laplace and the Stokes equation.

2.4.1 BIE for the Laplace equation

In this section we turn the Laplace equation, considered into a domain D with boundary C, into the integral form. To do so, we introduce the Green's second identity

$$\psi \nabla^2 w - w \nabla^2 \psi = \nabla \cdot (\psi \nabla w - w \nabla \psi), \tag{2.16}$$

where ψ is an arbitrary scalar function. Usually we set $\psi = G$, where G is the Green's function for the Laplace equation; by definition G satisfy the singularity forced Laplace's equation

$$\nabla^2 G(\mathbf{x}, \mathbf{x_0}) + \delta(\mathbf{x} - \mathbf{x_0}) = 0, \tag{2.17}$$

where

- $\mathbf{x} = (x, y)$ is the coordinate vector.
- $\mathbf{x_0} = (x_0, y_0)$ is a specific point into the domain called *pole* or *singularity point* or just the *singularity*.
- $\delta(\mathbf{x} - \mathbf{x_0})$ is the Dirac's delta function in two dimensions.

In the next step, we integrate the Green's second identity 2.16 over the domain $D' = D - D_\epsilon$, sketched in figure 2.5; in fact we delete from D a small disk D_ϵ of radius ϵ and centered at $\mathbf{x_0}$, to avoid the enclosing of the point $\mathbf{x} = \mathbf{x_0}$, which does not belong to the Green's function domain.

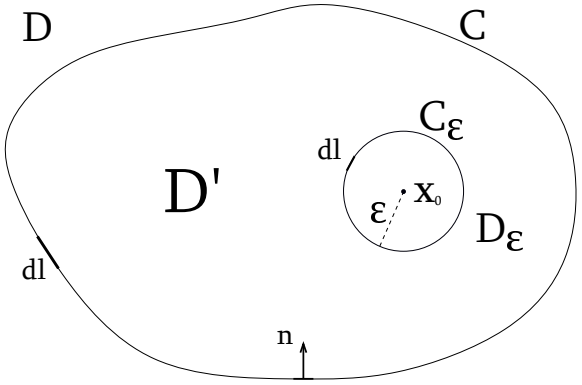

Figure 2.5: Domain of integration D'.

$$\iint_{D'} (G\nabla^2 w - w\nabla^2 G)dS = \iint_{D'} \nabla \cdot (G\nabla w - w\nabla G)dS. \tag{2.18}$$

Left-hand side of the equation 2.18 is equal to zero, since $\nabla^2 w = 0$, and $\nabla^2 G = 0$ when $\mathbf{x} \neq \mathbf{x_0}$ because of the Dirac's delta function properties. Applying the divergence theorem at the left-hand side of the equation 2.18 we obtain

$$\int_{C+C_\epsilon} (G\nabla w - w\nabla G) \cdot \mathbf{n} dl = 0, \tag{2.19}$$

where C is the boundary to D, C_ϵ is the boundary to D_ϵ, and l measures arc length along either C or C_ϵ. Considering the integral along C_ϵ and defining $r = |\mathbf{x} - \mathbf{x_0}|$, this expression can be simplified substituting the scalar product between $\mathbf{n}$ and both the gradients, with the r-derivative as follow

$$I_\epsilon = \int_{C_\epsilon} (G\nabla w - w\nabla G) \cdot \mathbf{n} dl = \int_{C_\epsilon} (G\frac{\partial w}{\partial r})dl - \int_{C_\epsilon} w\frac{\partial G}{\partial r} dl, \tag{2.20}$$

This passage can be done because C_ϵ is a circumference with normal $\mathbf{n}$. When $\mathbf{x} \neq \mathbf{x_0}$ or $r \neq 0$ the singular forced Laplace's equation become $\nabla^2 G = 0$, and assuming G dependent only on r, it can be found that the solution reads

$$G = \lambda \log r, \tag{2.21}$$

where λ is an arbitrary constant. This fundamental solution of the equation 2.17 is called *free-space Green's function*. We can employ the free-space Green's function in

order to simplify the expression of I_ϵ, in fact, substituting 2.21 into 2.20, we obtain

$$I_\epsilon = \int_{C_\epsilon} (\lambda \log r \frac{\partial w}{\partial r}) dl - \int_{C_\epsilon} w \frac{\lambda}{r} dl. \tag{2.22}$$

Since the radius of the circumference is equal to ϵ, and the integral is performed on the circumference, it is possible to substitute r with ϵ, moreover, letting $\epsilon \to 0$ we find

$$I_\epsilon = \lambda \log \epsilon \frac{\partial w(\mathbf{x_0})}{\partial r} \int_{C_\epsilon} dl - w(\mathbf{x_0}) \frac{\lambda}{\epsilon} \int_{C_\epsilon} dl =$$

$$= \lambda \log \epsilon \frac{\partial w(\mathbf{x_0})}{\partial r} 2\pi\epsilon - w(\mathbf{x_0}) \frac{\lambda}{\epsilon} \pi\epsilon = -2\pi\lambda w(\mathbf{x_0}). \tag{2.23}$$

Returning to the equation 2.19, we can substitute the integral on C_ϵ with the 2.23, and choose $\lambda = -1/2\pi$. We derive the velocity w from equation 2.19, that become the Boundary Integral Equation (BIE) for potential flow

$$w(\mathbf{x_0}) = \int_C w(\mathbf{x}) \mathbf{n} \cdot \nabla G(\mathbf{x}, \mathbf{x_0}) dl - \int_C G(\mathbf{x}, \mathbf{x_0}) \mathbf{n} \cdot \nabla w(\mathbf{x}) dl, \tag{2.24}$$

This is the integral formulation for the Laplace equation; the first integral on the right-hand side is called *Double-Layer Potential* (DLP) and the second one is called *Single-Layer Potential* (SLP). The equation 2.24 can be used to solve the longitudinal problem, and find the velocity field w in all the domain. We note that on the right-hand side, the unknown function w appears inside integrals which are defined over the boundary C. So the right-hand side involve only the boundary value of w. In general when a differential problem must be solved, the boundary condition are provided and this suggest the following way to proceed, that represent the heart of boundary integral method:

1. Take the point $\mathbf{x_0}$ to lie on the boundary C. Then the integral equation involves only values on the boundary.

2. Solve the integral equation for the unknowns boundary values, that depends by the boundary condition provided.

3. Compute the right-hand side of 2.24 in order to find w anywhere in the domain.

The first step require us to take the singularity to lie on C. It can be shown that the SLP is continuous as the point $\mathbf{x_0}$ approaches and then crosses C, in contrast, as $\mathbf{x_0}$ crosses C, the DLP undergoes a jump discontinuity. In order to find an expression for DLP when $\mathbf{x_0}$ lie on C, we take the limit $\mathbf{x_0} \to C$ and find

$$DLP = \int_C^{PV} w(\mathbf{x})\mathbf{n} \cdot \nabla G(\mathbf{x}, \mathbf{x_0}) dl \pm \frac{1}{2} w(\mathbf{x_0}), \tag{2.25}$$

where PV indicates that we are taking the principal value of the integral. If $\mathbf{x_0}$ approaches the boundary from the inside plus sign is valid, and if it approaches from the outside it must be chosen the minus sing. Supposing to be in the former situation, we can substitute 2.25 in 2.24 in order to obtain the boundary integral equation with $\mathbf{x_0}$ lying on the boundary

$$\frac{1}{2} w(\mathbf{x_0}) = \int_C^{PV} w(\mathbf{x})\mathbf{n} \cdot \nabla G(\mathbf{x}, \mathbf{x_0}) dl - \int_C G(\mathbf{x}, \mathbf{x_0})\mathbf{n} \cdot \nabla w(\mathbf{x}) dl. \tag{2.26}$$

This equation only involves values on the boundary of the domain. The second step deals with the solution of the equation 2.26 and there are three possible situations depending on the boundary condition

- Dirichlet boundary condition: equation 2.26 is used to obtain the values of the ∇w on the boundary.
- Neumann boundary condition: equation 2.26 is used to obtain the values of w on the boundary
- Robin boundary condition: equation 2.26 is used to obtain the value of ∇w where is given the values of w and viceversa.

Once the step two is done, it is possible to solve equation 2.24 for the unknown $w(\mathbf{x_0})$ with $\mathbf{x_0} \in D$. It can be highlighted the principal feature of the BIM: the value of the velocity in a specific point in the domain can be found using only the boundary values, without solving for all the domain.

2.4.2 BIE for the Stokes equation

As well as for Laplace's equation, we have to find the integral representation of the Stokes equation

$$\frac{\partial p}{\partial x_i} = \mu \frac{\partial^2 u_i}{\partial x_j \partial x_j}. \tag{2.27}$$

We use the Lorentz reciprocal relation, that has the same role of the second Green's identity 2.16 presented in the previous section

$$\frac{\partial}{\partial x_j}\left(u_i' \sigma_{ij} - u_i \sigma_{ij}'\right) = 0. \tag{2.28}$$

u_i' and σ_{ij}' are respectively the velocity vector and the stress tensor of a Stokes flow, whereas u_i and σ_{ij} are again the same quantities but for another different Stokes flow. To derive the boundary integral representation of two dimensional Stokes flow, we apply this identity for a particular Stokes flow of interest with velocity vector u_i and stress tensor σ_{ij} and for the flow due to a point force (u_i', σ_{ij}'). The velocity and stress tensor of the latter flow corresponds to the solution of the singularity forced Stokes differential equation

$$\frac{\partial p'}{\partial x_i} - \mu \frac{\partial^2 u_i'}{\partial x_j \partial x_j} + b_i \delta(\mathbf{x} - \mathbf{x_0}) = 0, \tag{2.29}$$

where b_i stands for the i-th component of the constant vector that determines the strength and orientation of the point force. As described in the previous section, the solutions of a singularity forced equation are called Green's function, hence we can define the velocity Green's function and the pressure Green's function which are the solution fields of equation 2.29

$$u_i'(\mathbf{x}) = \frac{1}{4\pi\mu} G_{ij}(\mathbf{x}, \mathbf{x_0}) b_j, \qquad p'(\mathbf{x}) = \frac{1}{4\pi} p_j(\mathbf{x}, \mathbf{x_0}) b_j. \tag{2.30}$$

G_{ij} is a second order tensor called velocity Green's function and p_j a vector called pressure Green's function. The stress tensor in equation 2.30 can be expressed using the constitutive law for a Newtonian fluid, which reads

$$\sigma_{ij}' = -\delta_{ij} p' + \mu \left(\frac{\partial u_i'}{\partial x_j} + \frac{\partial u_j'}{\partial x_i} \right). \tag{2.31}$$

Substituting the equations 2.30 into the 2.31, we obtain a representation of the stress tensor in terms of velocity and pressure Green function

$$\sigma'_{ij} = \frac{1}{4\pi}\left[-\delta_{ij}p_k + \frac{\partial G_{ik}}{\partial x_j} + \frac{\partial G_{jk}}{\partial x_i}\right] b_k. \tag{2.32}$$

For convenience, we define the following tensor

$$T_{ijk} = \frac{1}{4\pi}\left[-\delta_{ij}p_k + \frac{\partial G_{ik}}{\partial x_j} + \frac{\partial G_{jk}}{\partial x_i}\right], \tag{2.33}$$

thus

$$\sigma'_{ij}(\mathbf{x}) = T_{ijk}(\mathbf{x}, \mathbf{x_0})b_k. \tag{2.34}$$

We can now substitute the relation 2.30 and 2.34 into the Lorentz relation 2.28, and dropping the vector $b_j/4\pi$ we obtain

$$\frac{\partial}{\partial x_j}\left(G_{ik}\sigma_{ij} - \mu u_i T_{ijk}\right) = 0. \tag{2.35}$$

In the next step, we integrate 2.35 over a domain $D' = D - D_\epsilon$, sketched in figure 2.5, and use the divergence theorem, obtaining

$$\iint_{D'} \frac{\partial}{\partial x_j}\left(G_{ik}\sigma_{ij} - \mu u_i T_{ijk}\right) dS =$$

$$= \int_{C'} \left(G_{ik}\sigma_{ij} - \mu u_i T_{ijk}\right) n_j dl = 0. \tag{2.36}$$

Since the boundary of D' is $C' = C + C_\epsilon$, the linearity of the integral allow us to split the left-hand of 2.36 in an integral performed on C and another integral performed on C_ϵ. In order to simplify equation 2.36, we take under consideration the latter expressed in polar coordinates

$$I_\epsilon = \int_0^{2\pi} \left(G_{ik}\sigma_{ij} - \mu u_i T_{ijk}\right) n_j r d\theta, \tag{2.37}$$

and we take the limit $\epsilon \to 0$. Before to proceed with the limit we do some considerations. The integration domain of 2.37 corresponds to the circumference of radius ϵ, hence the relation $\epsilon = |\mathbf{x} - \mathbf{x_0}|$ is valid, and therefore, the limit $\epsilon \to 0$ means that $\mathbf{x}$ moves closer to $\mathbf{x_0}$, or mathematically, $\mathbf{x} \to \mathbf{x_0}$. If we examine G_{ij} and T_{ijk} as $\mathbf{x} \to \mathbf{x_0}$,

we find out that these always behave respectively as a stokeslet velocity Green's function and a stokeslet stress Green's function, which read respectively as follows

$$G_{ij} = \delta_{ij}\log r + \frac{\hat{x_i}\hat{x_j}}{r^2}, \qquad T_{ijk} = -4\frac{\hat{x_i}\hat{x_j}\hat{x_k}}{r^4}, \tag{2.38}$$

where $\hat{\mathbf{x}} = \mathbf{x} - \mathbf{x_0}$ and $r = |\mathbf{x} - \mathbf{x_0}| = \epsilon$. Employing all these consideration we can write

$$\lim_{\epsilon\to 0} I_\epsilon = \lim_{\epsilon\to 0} \int_{C_\epsilon} \left[\left(\delta_{ik}\log\epsilon + \frac{\hat{x_i}\hat{x_k}}{\epsilon^2} \right) \sigma_{ij} + 4\mu u_i \frac{\hat{x_i}\hat{x_j}\hat{x_k}}{\epsilon^4} \right] n_j \epsilon dr d\theta =$$

$$= \lim_{\epsilon\to 0} \int_{C_\epsilon} \left(\delta_{ik}\epsilon\log\epsilon + \frac{\hat{x_i}\hat{x_k}}{\epsilon} \right) \sigma_{ij} n_j + \int_{C_\epsilon} 4\mu u_i \frac{\hat{x_i}\hat{x_k}}{\epsilon^3} \hat{x_j} n_j dr d\theta. \tag{2.39}$$

Other simplifications can be achieved observing that

$$\lim_{\epsilon\to 0} \epsilon\log\epsilon = 0, \tag{2.40}$$

$$\hat{x_i}\hat{x_k} \sim \epsilon^2 \Rightarrow \lim_{\epsilon\to 0} \frac{\hat{x_i}\hat{x_k}}{\epsilon} = 0, \tag{2.41}$$

$$\mathbf{n} = \frac{\mathbf{x} - \mathbf{x_0}}{|\mathbf{x} - \mathbf{x_0}|} = \frac{\hat{\mathbf{x}}}{\epsilon} \Rightarrow n_j = \frac{\hat{x_j}}{\epsilon} \Rightarrow \hat{x_j} n_j = \frac{\hat{x_j}\hat{x_j}}{\epsilon} = \frac{|\hat{\mathbf{x}}|^2}{\epsilon} = \frac{\epsilon^2}{\epsilon} = \epsilon. \tag{2.42}$$

Applying these three relations to the equation 2.39, we have

$$\lim_{\epsilon\to 0} I_\epsilon = \lim_{\epsilon\to 0} \int_{C_\epsilon} 4\mu u_i \frac{\hat{x_i}\hat{x_k}}{\epsilon^2} d\theta. \tag{2.43}$$

We remembering that u_i is a function of $\mathbf{x}$, and $\epsilon \to 0$ (i.e. $\mathbf{x} \to \mathbf{x_0}$), therefore

$$\lim_{\epsilon\to 0} u_i(\mathbf{x}) = u_i(\mathbf{x_0}). \tag{2.44}$$

The i-th component of the velocity vector computed in the singularity is a constant, and it can drop the integral

$$\lim_{\epsilon\to 0} I_\epsilon = \lim_{\epsilon\to 0} 4\mu u_i(\mathbf{x_0}) \int_{C_\epsilon} \frac{\hat{x_i}\hat{x_k}}{\epsilon^2} d\theta \tag{2.45}$$

We use this result in order to rearrange the relation 2.36 and express the velocity vector computed on the singularity

$$u_i(\mathbf{x_0}) = \frac{1}{4\pi}\int_C u_i(\mathbf{x})T_{ijk}(\mathbf{x},\mathbf{x_0})n_j dl - \frac{1}{4\pi\mu}\int_C G_{ik}(\mathbf{x},\mathbf{x_0})\sigma_{ij}(\mathbf{x})n_j dl. \tag{2.46}$$

Equation 2.46 is the integral formulation for the Stokes equation, and in line with the integral formulation of the Laplace equation, we can call the terms on the right-end side DLP and SLP. Moreover, as we saw in section 2.4.1, we can put $\mathbf{x_0}$ on the boundary and derive an expression that involves only boundary quantities

$$\frac{1}{2}u_i(\mathbf{x_0}) = \frac{1}{4\pi}\int_C^{PV} u_i(\mathbf{x})T_{ijk}(\mathbf{x},\mathbf{x_0})n_j dl - \frac{1}{4\pi\mu}\int_C G_{ik}(\mathbf{x},\mathbf{x_0})\sigma_{ij}(\mathbf{x})n_j dl \tag{2.47}$$

The boundary conditions allow to solve equation 2.47, and subsequently the solution can be found in all the domain with the equation 2.46.

2.5 Boundary element method

The integral equations obtained for the longitudinal and the transverse problems are numerically solved. The numerical counterpart of the BIM is called *Boundary Element Method* (BEM), and generate a numerical solution of the integral equations. The numerical implementation of the BEM involves the following steps:

1. Discretize the boundary into a collection of discrete elements, and approximate the boundary integrals with the sum of the integrals over each the boundary segments.

2. Introduce an approximations for the unknown function over the individual boundary element.

3. Apply the integral equation at some collocation points located over the boundary elements

4. Perform the integration of the single- and double-layer potential over the boundary elements.

5. Solve the linear system for the unknown functions of at the collocation point.

In the next sections, we shell describe in details all these steps; the first one is the same for both the Laplace and Stokes equations (the geometry over which the equations are applied is the same), but all the next steps are slightly different. We have decided to show the application of the boundary element method only for the parallel problem; the application to the perpendicular problem is done in a similar fashion, however it is much harder because of the vectorial nature of the Stokes equation.

2.5.1 Boundary discretization

The boundary-element method derives its name from the practice of describing the boundary of a solution domain with a collection of elementary geometrical units called boundary elements. A variety of boundary elements are available in two dimensions. Three popular choices are linear elements with straight shapes, circular arcs, and elements of cubic splines. Since the last one is the most flexible in terms of representation of different geometries, we have decided to employ it in our implementation.

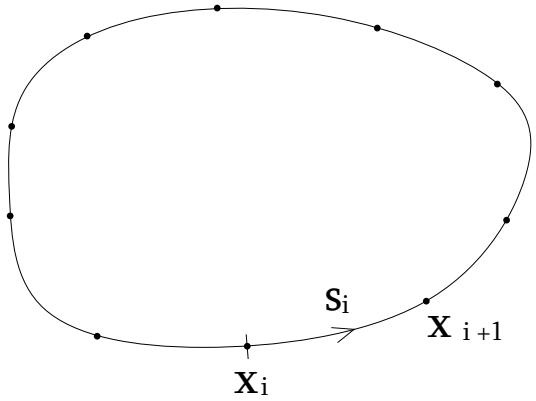

Figure 2.6: Example of the discretized domain.

To implement this discretization, let us describe the boundary with N nodes, and define s_i as the current length of the polygonal line connecting sequential nodes from the first node (arbitrarily chosen) to the i-th node. An example of the discretized domain is shown in figure 2.6. The i-th element of the discretization is between the i-th and the $(i+1)$-th node, and it can be described by the the cubic polynomial as

$$x_i(s) = a_i^x(s-s_i)^3 + b_i^x(s-s_i)^2 + c_i^x(s-s_i) + x_i^G,$$

$$y_i(s) = a_i^y(s-s_i)^3 + b_i^y(s-s_i)^2 + c_i^y(s-s_i) + y_i^G, \tag{2.48}$$

with $\mathbf{x}_i = (x_i^G, y_i^G)$ the global Cartesian coordinates of the i-th node and $s_i \leq s \leq s_{i+1}$ the curvilinear abscissa. Cubic spline discretization involves three unknown coefficients for each coordinate parametrization, therefore, we have six unknown coefficients for each elements. Since the number of elements is $N-1$, the total number of the unknown coefficients is $6(N-1)$. In order to fix all the coefficients, we impose the following three conditions for both the x- and y-coordinates; we report them only for the x-coordinate:

- the geometry continuity

$$x_i(s_{i+1}) = x_{i+1}^G \Rightarrow$$

$$\Rightarrow a_i^x h_i^3 + b_i^x h_i^2 + c_i^x h_i + x_i^G = x_{i+1}^G, \quad i = 1, ..., N-1 \tag{2.49}$$

- the slope continuity

$$\left.\frac{\mathrm{d}x_i}{\mathrm{d}s}\right|_{s_{i+1}} = \left.\frac{\mathrm{d}x_{i+1}}{\mathrm{d}s}\right|_{s_{i+1}} \Rightarrow$$

$$\Rightarrow 3a_i^x h_i^2 + 2b_i^x h_i + c_i^x = c_{i+1}^x, \quad i = 1, ..., N-2 \tag{2.50}$$

- the curvature continuity

$$\left.\frac{\mathrm{d}^2x_i}{\mathrm{d}s^2}\right|_{s_{i+1}} = \left.\frac{\mathrm{d}^2x_{i+1}}{\mathrm{d}s^2}\right|_{s_{i+1}} \Rightarrow$$

$$\Rightarrow 6a_i^x h_i + 2b_i^x + = 2b_{i+1}^x, \quad i = 1, ..., N-2 \tag{2.51}$$

where $h_i = s_{i+1} - s_i$. Rearranging properly these relations we can find the following relations for the unknown coefficients:

$$a_i = \frac{b_{i+1} - b_i}{3h_i}, \tag{2.52}$$

$$c_i = \frac{x_{i+1}^G - x_i^G}{h_i} - \frac{1}{3}h_i(b_{i+1} + 2b_i), \tag{2.53}$$

$$\frac{h_i}{3}b_i + 2\frac{h_i + h_{i+1}}{3}b_{i+1} + \frac{h_{i+1}}{3}b_{i+2} = \frac{x_{i+2}^G - x_{i+1}^G}{h_{i+1}} - \frac{x_{i+1}^G - x_i^G}{h_i}. \tag{2.54}$$

The system 2.54 involves $N-3$ equations, and the number of b-coefficients is $N-1$, therefore, two additional conditions are required. In this work we will take under consideration a closed boundary, hence we impose periodicity conditions for the first and second derivative at the first and last nodes expressed, respectively, by the equations

$$3a_{N-1}h_{N-1}^2 + 2b_{N-1}h_{N-1} + c_{N-1} = c_1 \tag{2.55}$$

$$b_N = b_1 \tag{2.56}$$

Now we can solve the system 2.54 and subsequently determine a and b-coefficients through the relations 2.53. After these passages all the coefficients are known, and hence the polynomial for each element of the discretization is known. After the discretization of the boundary, whatever kind it is, we can exploit the linearity of the integral in order to obtain a discrete representation of the boundary integral equations:

[1]

$$w(\mathbf{x_0}) = \sum_{i=1}^{N} \int_{E_i} w(\mathbf{x}) \mathbf{n} \cdot \nabla G(\mathbf{x}, \mathbf{x_0}) dl - \sum_{i=1}^{N} \int_{E_i} G(\mathbf{x}, \mathbf{x_0}) \mathbf{n} \cdot \nabla w(\mathbf{x}) dl, \tag{2.57}$$

$$\frac{1}{2} w(\mathbf{x_0}) = \sum_{i=1}^{N} \int_{E_i} w(\mathbf{x}) \mathbf{n} \cdot \nabla G(\mathbf{x}, \mathbf{x_0}) dl - \sum_{i=1}^{N} \int_{E_i} G(\mathbf{x}, \mathbf{x_0}) \mathbf{n} \cdot \nabla w(\mathbf{x}) dl. \tag{2.58}$$

Next step deal with the interpolation of the unknown functions inside the integrals.

2.5.2 Approximation of the boundary quantities

Once the boundary discretization is completed, we can pass to the second step of the boundary element method: the approximation of the unknown quantities which appear inside the integrals (i.e., in the case of Laplace's equation, $w(\mathbf{x})$ and $\nabla w(\mathbf{x})$). The approximation aims at writing the unknown functions through their value evaluated to specific points of the boundary. Thereby, integral equations become a linear algebraic system, and, as we shell explain, it can be numerically solved. Before proceeding with the approximation, it is important to map the global coordinate $\mathbf{x}$ into the local coordinate $\xi \in [-1, 1]$ defined over each element. This is a necessary condition for the numerical calculation of the integrals. To do so, we start by expressing the integrand function in term of the curvilinear abscissa defined over an element E_i

$$DLP_i = \int_{E_i} w(\mathbf{x}) \mathbf{n} \cdot \nabla G(\mathbf{x}, \mathbf{x_0}) dl = \int_{s_i}^{s_{i+1}} w[\mathbf{x}(s)] \mathbf{n} \cdot \nabla G[\mathbf{x}(s), \mathbf{x_0}] h_i(s) ds, \tag{2.59}$$

$$SLP_i = \int_{E_i} G(\mathbf{x}, \mathbf{x_0}) \mathbf{n} \cdot \nabla w(\mathbf{x}) dl = \int_{s_i}^{s_{i+1}} G[\mathbf{x}(s), \mathbf{x_0}] \mathbf{n} \cdot \nabla w[\mathbf{x}(s)] h_i(s) ds, \tag{2.60}$$

where $h_i(s)$ is the metric associated with the i-th element, while s_i and s_{i+1} are the polygonal arch lengths of the element at starting and ending points respectively. For a cubic spline element, calling $\Delta s = s - s_i$ the metric coefficients takes the form:

$$h_i(s) = \sqrt{\left(\frac{\mathrm{d}x_i}{\mathrm{d}s}\right)^2 + \left(\frac{\mathrm{d}y_i}{\mathrm{d}s}\right)^2} =$$

$$= \sqrt{(3a_i^x \Delta s^2 + 2b_i^x \Delta s + c_i^x)^2 + (3a_i^y \Delta s^2 + 2b_i^y \Delta s + c_i^y)^2}. \tag{2.61}$$

[1] The same passages can be done for the stokes integral equation.

We apply another coordinate transformation which maps an element from the global coordinate system based on the curvilinear abscissa to a local coordinate system such that the i-th element's boundary points are mapped into the inteval $[-1, 1]$. This mapping will can be simply done using the following relation

$$s_i(\xi) = \frac{s_{i+1} + s_i}{2} + \frac{s_{i+1} + s_i}{2}\xi = s_i^m + s_i^d\xi, \tag{2.62}$$

from which we can easily define the associated metric $h_i^\xi = s_i^d$. Introducing this new parametrization into the integrals 2.59 and 2.60 we obtain:

$$DLP_i = h_i^\xi \int_{-1}^{1} w[\mathbf{x}(s(\xi))]\mathbf{n} \cdot \nabla G[\mathbf{x}(s(\xi)), \mathbf{x_0}]h_i(s(\xi))d\xi =$$

$$= h_i^\xi \int_{-1}^{1} w(\xi)\mathbf{n} \cdot \nabla G[\xi, \mathbf{x_0}]h_i(\xi)d\xi, \tag{2.63}$$

$$SLP_i = h_i^\xi \int_{-1}^{1} G[\mathbf{x}(s(\xi)), \mathbf{x_0}]\mathbf{n} \cdot \nabla w[\mathbf{x}(s(\xi))]h_i(s(\xi))d\xi =$$

$$= h_i^\xi \int_{-1}^{1} G[\xi, \mathbf{x_0}]\mathbf{n} \cdot \nabla w(\xi)h_i(\xi)d\xi. \tag{2.64}$$

Until now, no assumption about the interpolation method of the unknown functions over the element has been done. For our purposes, we propose to use a piecewise linear variation, which is a good compromise between accuracy and programming difficulty; thus let us consider the function $w(\xi)$ for the i-th element in the following linear approximation

$$w_i(\xi) \approx \frac{w(\xi_2) - w(\xi_1)}{\xi_2 - \xi_1}(\xi - \xi_1) + w(\xi_1) =$$

$$= w_i(\xi_1)\left(\frac{\xi_1 - \xi}{\xi_2 - \xi_1} + 1\right) + w(\xi_2)\left(\frac{\xi - \xi_1}{\xi_2 - \xi_1}\right) =$$

$$= \Psi_1(\xi)w_i(\xi_1) + \Psi_2(\xi)w_i(\xi_2), \tag{2.65}$$

with ξ_1 and ξ_2 the two collocation points where the function is evaluated on the i-th element, and $\Psi_1(\xi)$ and $\Psi_2(\xi)$ the two shape functions. The same linear approximation can be written for the function $f = \nabla w(\mathbf{x})$

$$f_i(\xi) \approx \Phi_1(\xi)f_i(\xi_1) + \Phi_2(\xi)f_i(\xi_2). \tag{2.66}$$

For the seek of simplicity, we call

$$w_{i1} = w_i(\xi_1), \qquad w_{i2} = w_i(\xi_2), \qquad f_{i1} = f_i(\xi_1), \qquad f_{i2} = f_i(\xi_2), \tag{2.67}$$

and, substituting the equation 2.65 and 2.66 respectively into the double and single layer potential, we obtain

$$DLP_i = h_i^{\xi} \left(w_{i1} \int_{-1}^{1} \Psi_1 \mathbf{n} \cdot \nabla G h_i d\xi + w_{i2} \int_{-1}^{1} \Psi_2 \mathbf{n} \cdot \nabla G h_i d\xi \right). \tag{2.68}$$

$$SLP_i = h_i^{\xi} \left(f_{i1} \int_{-1}^{1} \Phi_1 G h_i d\xi + f_{i2} \int_{-1}^{1} \Phi_2 G h_i d\xi \right) \tag{2.69}$$

It is possible to note that all the functions inside the integrals of the 2.68 and 2.69 are known, therefore the integrals can be computed numerically, and the two relations become linear. It is now possible to define the influence coefficient as as follows

$$W_i^1 = h_i^{\xi} \int_{-1}^{1} \Psi_1 \mathbf{n} \cdot \nabla G h_i d\xi, \qquad W_i^2 = h_i^{\xi} \int_{-1}^{1} \Psi_2 \mathbf{n} \cdot \nabla G h_i d\xi,$$

$$F_i^1 = h_i^{\xi} \int_{-1}^{1} \Phi_1 G h_i d\xi, \qquad F_i^2 = h_i^{\xi} \int_{-1}^{1} \Phi_2 G h_i d\xi, \tag{2.70}$$

and substituting equations 2.68 and 2.69 in the equation 2.58, it is possible to write the final equation derived by the discretization of the boundary and the piecewise linear approximation of the unknown functions on the boundary. At the end of the procedure we have

$$\frac{1}{2} w(\mathbf{x_0}) = \sum_{i=1}^{N} \left(w_{1i} W_i^1 + w_{2i} W_i^2 \right) - \sum_{i=1}^{N} \left(f_{1i} F_i^1 + f_{2i} F_i^2 \right). \tag{2.71}$$

To the left-hand side of the equation 2.71 the function w is evaluated in $\mathbf{x_0}$, that we have chosen to lie on the boundary. This means that all the functions in equation 2.71 are to be evaluated on the boundary, and this is the specific feature that will allow us to solve the equation.

It is now worth to note the role of collocation points, which are the points in which the two unknown functions will be evaluated (i.e. the solution of the linear system will give us the value of the unknown functions in all the collocation points on the boundary). In general we will choose two collocation points for each element,

laying respectively at the beginning and at the end of the segment. However, there is the special case of a corner, for which the choice of them is a bit different. When a boundary element is adjacent to a true boundary corner (but not an artificial corner due to the discretization), the boundary distribution of the function f and its normal derivative are likely to exhibit discontinuous or singular behavior, and a continuous distribution of those quantities is no more appropriate. The used approach involves distributing the near-corner nodes at positions corresponding to the roots of the Radau polynomials defined over the interval $[-1, 1]$. The first few members of this family are

$$R_0(\xi) = 1, \qquad R_1(\xi) = \frac{1}{2}(3\xi - 1) \qquad R_2(\xi) = \frac{1}{2}(5\xi^2 - 2\xi - 1)$$

$$R_3(\xi) = \frac{1}{8}(35\xi^3 - 15\xi^2 - 15\xi + 3) \tag{2.72}$$

Since we choose the linear approximation of the function, we will use the R_1 polynomial.

The boundary conditions fix the all the quantities computed on the boundary. In the end, we can locate the singularity in different points, in order to obtain the same number of equation and unknowns. A solvable linear system of equations has been obtained.

2.5.3 Singular integrals

All the integral involved in the computation of the influence coefficients F_{ij} and the known terms W_j are numerically solved with the well known Gauss-Legedre method. However, we have to pay attention to some particular integrals, that result to be singular.

The j-th line of the system represent the equation obtained from the positioning of the singularity on the j-th element. In order to compute the coefficients of this j-th row of the matrix F, we have to numerically solve for each element the integrals given by the equations 2.70. The problem of the singular integral arise when the element on which the integration is performed, is the same on which the singularity lies. We deal with this situation when the subscript i (that identify the element) is equal to j (that identify the element on which the singularity lie). The singular behaviour of the integrals is due to the presence of the Green's function (inside the F coefficients) and

its gradient (inside the W coefficients) inside them. In fact it is possible to write

$$\mathbf{x} \to \mathbf{x_0} \Rightarrow \begin{cases} G \to +\infty \\ \nabla G \to +\infty \end{cases} \tag{2.73}$$

Singular integrals need a special treatment; to compute them we add and subtract the free-space kernels in the integrand and split the expression of F and W coefficients in two integrals

$$F_{jj} = \int_{E_j} \left(G(\mathbf{x}, \mathbf{x_0}) + \frac{1}{2\pi} \ln |\mathbf{x} - \mathbf{x_0}| \right) \mathrm{d}l - \frac{1}{2\pi} \int_{E_j} \ln |\mathbf{x} - \mathbf{x_0}| \, \mathrm{d}l, \tag{2.74}$$

$$W_j = \int_{E_j}^{PV} \left(\mathbf{n} \cdot \nabla G(\mathbf{x}, \mathbf{x_0}) + \frac{1}{2\pi} \frac{\mathbf{n} \cdot (\mathbf{x} - \mathbf{x_0})}{|\mathbf{x} - \mathbf{x_0}|^2} \right) \mathrm{d}l - \frac{1}{2\pi} \int_{E_j}^{PV} \frac{\mathbf{n} \cdot (\mathbf{x} - \mathbf{x_0})}{|\mathbf{x} - \mathbf{x_0}|^2}. \tag{2.75}$$

The first integrals on the right-hand side of the 2.74 and 2.75 are non-singular and may be computed with high accuracy using Gauss-Legendre quadrature. Moreover, even the second integral on the right-hand side of the equation 2.75 is non-singular, in fact, as the integration point $\mathbf{x}$ approach the singularity $\mathbf{x_0}$, the normal vector n tends to became to the nearly tangential vectorial distance $(\mathbf{x} - \mathbf{x_0})$. Consequently, the numerator of the fraction of the integrand behaves quadratically with respect to the scalar distance $|\mathbf{x} - \mathbf{x_0}|$, and the singularity does not appear.

Thus the problem has been reduced to compute the second integral of the right-hand side of the equation 2.74. The treatment of this term depend on the kind of the element discretization, so we shell describe the procedure for the cubic-spline elements. In order to compute the kernel in F_{jj} we express it in the parametric form an

$$k = \int_{E_j} \ln |\mathbf{x} - \mathbf{x_0}| \, \mathrm{d}l = \int_{s_j}^{j+1} \ln |\mathbf{x}(s) - \mathbf{x}(s_0)| \, h_i(s) \mathrm{d}s, \tag{2.76}$$

where s_0 represents the singularity position ($s_j < s_0 < s_{j+1}$). Now it is possible to split the integral with the following passage

$$k = \int_{s_j}^{j+1} \ln \left(\frac{|\mathbf{x}(s) - \mathbf{x}(s_0)|}{|s - s_0|} \right) h_i(s) \mathrm{d}s + \int_{s_j}^{j+1} \ln |s - s_0| \, h_i(s) . \mathrm{d}s \tag{2.77}$$

In this case the first member can be integrated with numerical procedures, but the

second one remains singular. Therefore the afterwards treatment is necessary.

$$\int_{s_j}^{j+1} \ln|s - s_0|\, h_i(s)\mathrm{d}s =$$

$$= \int_{s_j}^{j+1} \ln|s - s_0|\, (h_i(s) - h_i(s_0))\, \mathrm{d}s + h_i(s_0) \int_{s_j}^{j+1} \ln|s - s_0|\, \mathrm{d}s. \tag{2.78}$$

The first member is numerically integrated, whereas the second one can be computed by elementary analytical method.

2.5.4 Matlab algorithm description

In order to solve the longitudinal and the transverse problem, the boundary element method has been implemented in Matlab. In this section we will explain the features of the input that the code receives and the output that it return, moreover, the method by which the protrusion heights are computed is explained.

The code take in input the coordinates of a series of points that describes the board of the domain taken under consideration. In particular each point represents the limit of a segment used to discretize the geometry of the domain. For example, in figure 2.7 it is possible to observe the domain and the points used to discretize it.

First of all it is important to note that both the lateral sides of the domain are not covered by points. In fact, the code take into account the periodicity of the riblet exploiting the periodic Green function 2.79, and not through the boundary conditions.

$$G = -\frac{1}{4\pi} \log\left\{2\left[\cosh\left(k(y - y_0)\right) - \sinh\left(k(x - x_0)\right)\right]\right\} \tag{2.79}$$

where $k = 2\pi/L$, and L is the period of the Green function. Obviously, the period of the Green function must coincide with the period of the riblet. It has been chosen $L = 1$, therefore the geometrical parameter that yields the riblet geometry dimensionless is the period. Moreover, it is possible to observe that the distribution of points in figure 2.7 is not uniform, and they increase near the edges. This kind of distribution is fundamental because allows to reduce the error due to the absence of the points that lay on the edges. In the end, The upper part of the domain must be theoretically located at an infinitely distance from the wall. From a practical point of view, the

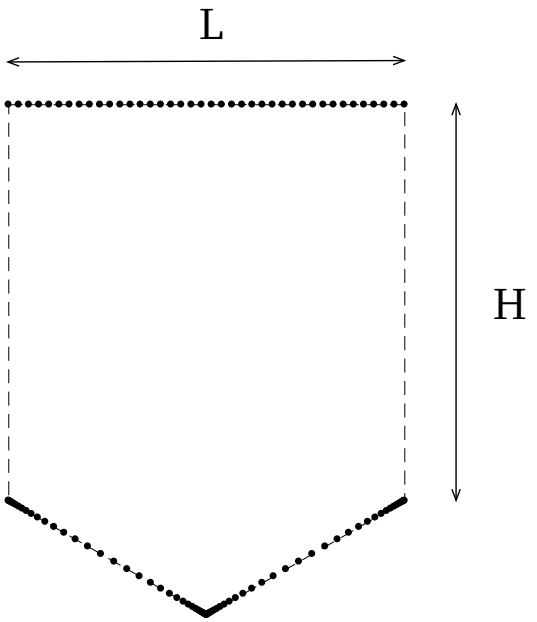

Figure 2.7: Domain border and discretization points.

upper side must not influence the flow near the wall, and to do so the code shift it sufficiently up.

Once the algorithm has taken in input such a geometry, it compute the values on the boundary of the domain; in particular it compute the value of the gradient of the velocity on the lower wall (in fact the velocity is here defined by the no-slip condition), and the velocity on the upper boundary (in fact the gradient of the velocity is hear defined equal to one). This last goal allow us to compute the protrusion heights. Before to proceed with the explanation of the computation of the protrusion heights, we have to note that the code can even compute the velocity inside all the domain; to do so it is possible to given in input a grid of point [2] and the code will compute the velocity on it.

Regarding the protrusion heights, the parallel one has been computed through the equation 2.80 and the perpendicular one through the equation 2.81.

$$h_{\parallel} = \frac{\dfrac{w_{\text{top}}}{\partial w/\partial y\Big|_{\text{top}}} - H}{L} \tag{2.80}$$

[2]It is interesting to note that the grid can be done without respect any principle.

$$h_\perp = \frac{\dfrac{v_{\text{top}}}{\partial v/\partial y\Big|_{\text{top}}} - H}{L} \tag{2.81}$$

where the subscript 'top' indicates that the parameter is computed on the upper side of the boundary, L is the period of the riblet geometry (set equal to one) and H is the distances between the tip of the riblet and the upper side of the boundary. The boundary condition set to one both the y-derivatives. The expressions for the protrusion heights can be easily derived from the definition given in the section 2.3: the protrusion height is the distance between the riblet tip and the point where the velocity become zero. Both expressions 2.80 and 2.81 can be understood looking at the figure reported below

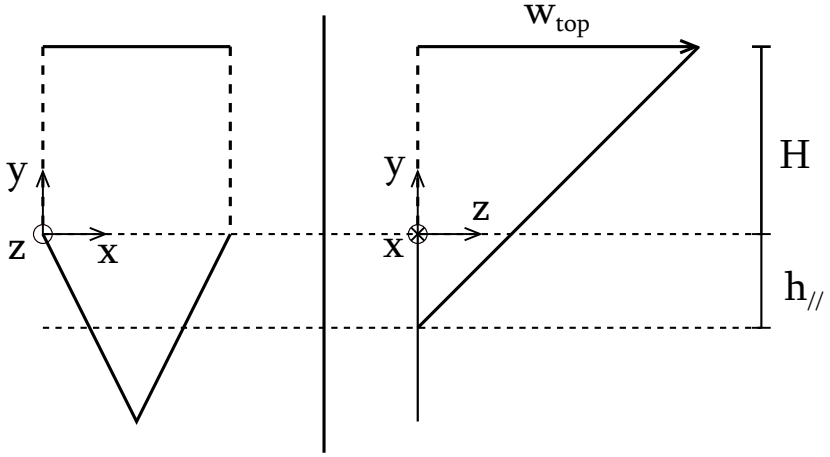

Figure 2.8: Computed protrusion height.

2.6 Validation of the code

Before to proceed with the simulations, it is important to validate the code; in other words we have to check that our code works. To do so, we have to compute an already solved case present in the literature and compare the results. If our calculation will be in accordance with the literature, our code will be validated. For this goal we study the riblet shape shown in figure 2.9

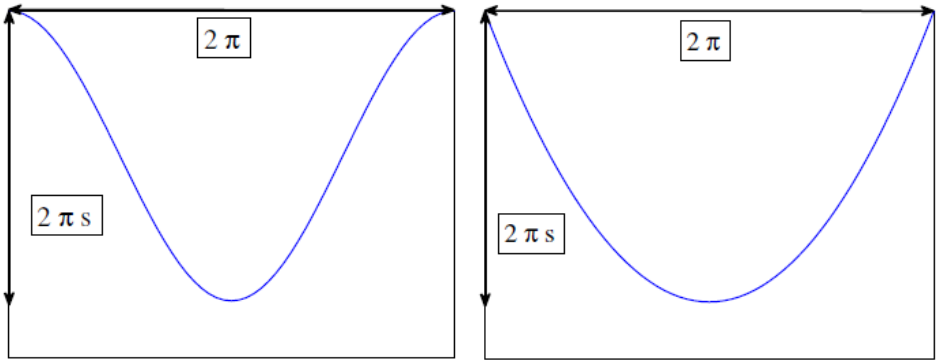

(a) Cosinus riblet. *(b)* Parabolic riblet.

Figure 2.9: Riblet shapes used for the validation.

they are described by the following relations

$$y_0 = \frac{2s}{\pi}x^2 - 4sx, \qquad y_0 = \pi s \cos x - \pi s \tag{2.82}$$

where s represent the ratio between the depth and the period of the riblet, and $0 \leq x \leq 2\pi$. These riblets have been studied by Luchini [20]; he has implemented the boundary element method (though with a different mathematical approach in the calculation of the transverse protrusion height), and he has computed the transverse and the longitudinal protrusion heights in function of s, as shown in figure 2.10.

First of all we can note that the results of Luchini make sense. In fact, when $s = 0$ the riblet cavity disappear and all the protrusion heights are zero. Instead, when the s parameter becomes higher then one, the riblet cavities become deeper and the riblet effect start to work. When the depth of the riblet is too high, the protrusion heights do not depends on s anymore; this behavior can be recognized in the exponential trend of all the curves.

In order to validate our code, we have computed the protrusion heights for both the riblets in figure 2.9 and for some value of s; it is possible to observe from the figure 2.10 that our results are in perfect accordance with the Luchini's one. The code is therefore validated.

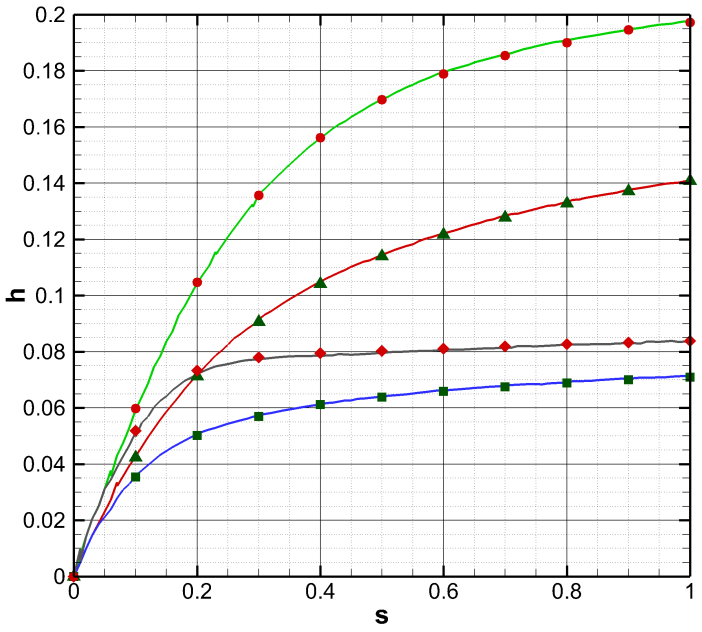

Figure 2.10: Validation against Luchini et al. [20]

2.7 Results

2.7.1 Constructed geometries

This work aim at computing the skin friction over a fractal riblet plates due to a turbulent flow, in particular, eight different riblet shapes have been built and simulated. All the constructed geometries are described in the following lines.

First of all it is worth to remember that the BEM solves the dimensionless equations 2.10 and 2.9, therefore, the geometries given in input to the code must be considered dimensionless. Moreover, we have chosen to build riblet geometries with period equal to one, and this imply that Stokes equation have been dimensionalized with the period (L). Two fractal geometries have been generated by the two different triangular mold sketched in figure 2.11a and figure 2.11b; the first one has an angle to the vertex of 120° (that imply $L/H = 0.29$, where H indicates the riblet cavity depth), and the second of 90° (that imply $L/H = 0.5$). These geometries have been built with a suitable CAD software and following the same steps used to build the Koch snowflake in section 1.3. For examples, in order to built the first fractal iteration both the sides of the triangular mold have been divided in three equal parts, and the resulting central segment has been substituted by an appropriately scaled original molds. The same procedure has been followed for the afterwards iterations. This type of construction is possible thanks to the self-similarity of the fractals. Once all the riblet shape have been carried out, we have used a suitable meshing software in order to obtain an optimal points distribution on the fractal shape. The distribution must in agreement with the rules described in section 2.5.4, thereby we can obtain an excellent approximation of the velocities in the corners. Doing so the points that describe each geometry are obtained and given in input to the Matlab code that implement the BEM.

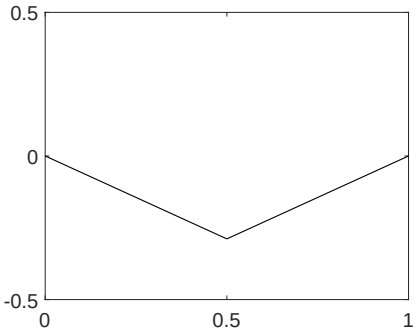

(a) 120° triangular mold.

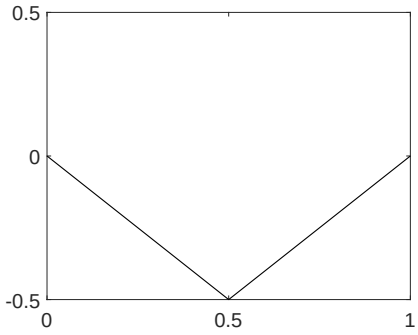

(b) 90° triangular mold.

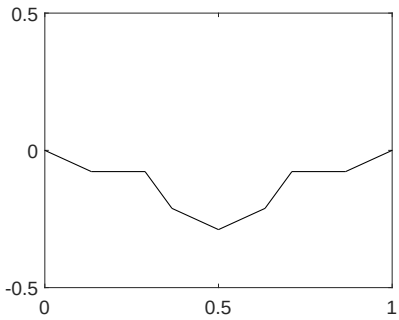

(c) First iteration of the 120° triangle.

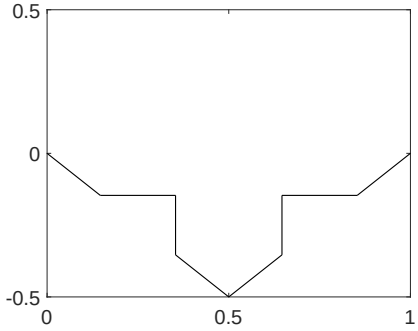

(d) First iteration of the 90° triangle.

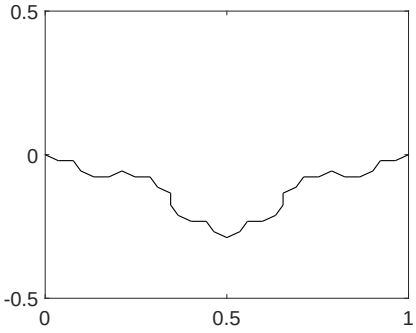

(e) Second iteration of the 120° triangle.

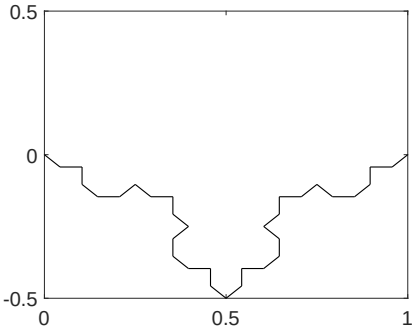

(f) Second iteration of the 90° triangle.

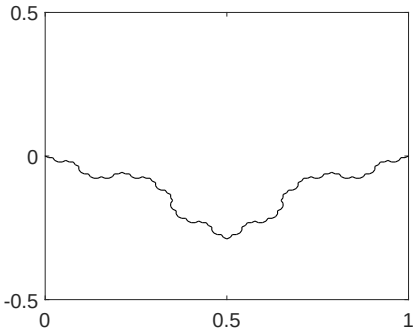

(g) Third iteration of the 120° triangle.

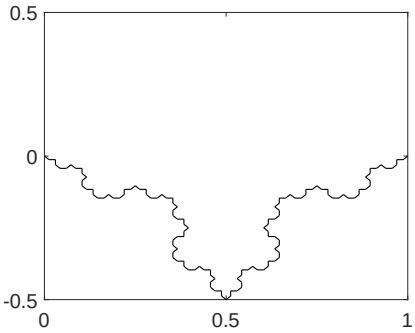

(h) Third iteration of the 90° triangle.

Figure 2.11: Fractals geometries under investigation.

2.7.2 120° triangle

In this section the results obtained for the triangular riblet (which has an angle to the vertex equal to 120°) sketched in figure 2.12a are shown.

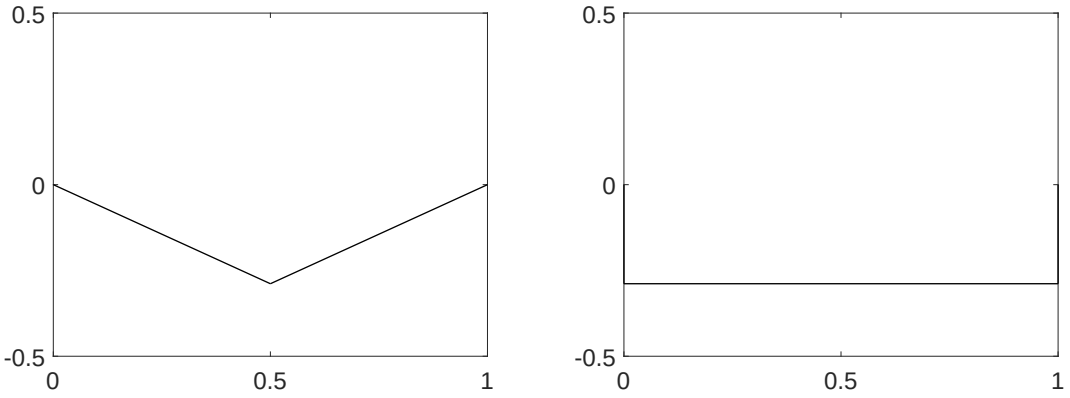

(a) Triangular riblet. *(b)* Blade riblet.

Figure 2.12: Geometries under investigation.

In order to have a reference value for the protrusion heights and the difference between them, we have taken under consideration the blade riblet sketched in figure 2.12b, with the same depth of the triangular one. In table 2.1 are reported the protrusion heights computed for the triangular and the rectangular riblet; the data shows that the Δh is higher in the blade riblet case.

Case	$h_{\|\|}$	$h_{\perp}$	Δh
Blade riblet	0.1723	0.0801	0.0922
Triangular riblet	0.1026	0.0704	0.0322

Table 2.1: Protrusion heights of blade-riblet and 120° triangular riblet.

In line with Luchini's theory, it is possible to understand that drag reduction achieved with the triangular riblet will be smaller then that obtained with the blade one. The result is in accordance with a lot of experiment performed on the two riblet shapes and even with the theoretical work by Bechert and Bartewerfer [27]. From a physical point of view, the viscous flow over triangular riblet geometry generates an higher skin friction then that over the blade riblet [1]. It is extremely interesting to note that the

triangular riblet wall surface is smaller then the blade riblet one, so that one expect an higher drag on the blade riblet. Therefore a viscous mechanism which compensate the area increase exist.

Now let us look to the results reported in table 2.2, they have been obtained applying the boundary element method at each fractal iteration of the 120° triangle show in figure 2.11a.

Iteration	$h_{\|\|}$	$h_{\perp}$	Δh
0	0.1026	0.0704	0.0322
1	0.0819	0.0604	0.0215
2	0.0755	0.0554	0.0201
3	0.0737	0.0541	0.0196

Table 2.2: Protrusion heights for all fractals iterations of the 120° triangle.

First of all it is important to note that

$$\frac{|\Delta h_3 - \Delta h_0|}{\Delta h_0} < \frac{|\Delta h_{\text{blade}} - \Delta h_0|}{\Delta h_0} \tag{2.83}$$

where Δh_3 and Δh_0 are the difference between the parallel and the perpendicular protrusion heights respectively of the iteration 3 and the iteration 0, whereas Δh_{blade} is that of the blade riblet. The blade riblet and the triangular one (iteration 0) generate a drag reduction that differs of a few percent points (about 5), and the difference between their Δh is $|\Delta h_{blade} - \Delta h_0| / \Delta h_0 = 1.86$. Since we have $|\Delta h_3 - \Delta h_0| / \Delta h_0 = 0.39$, it is possible to argue that the change in the drag obtained passing from the triangular to the fractal riblet will be small, and certainly not higher then a few percent points. The protrusion heights and the difference between them decrease going on with the iterations. The last trend is certainly due to a viscous effect, in fact the equations that allow us to compute the protrusion heights do not present the convective term. In other words the effect of the riblet shape on the protrusion height cannot be ascribed to the turbulence reduction. Therefore the microscopic feature of the riblet surface are capable to modify the viscous flow near the wall. It is even worth to clarify that the change in the viscous flow may affect the turbulence level, but protrusion height cannot

take into account such a modification. However, the aforementioned consideration does not exclude a possible relation between protrusion heights and the turbulence modification. Figure 2.13 and figure 2.14 reveal that the protrusions heights have an exponential behavior, and they approach a finite value. The motivation can be found in the dimension of the additional triangular pieces that are used to build each next fractal iteration. In fact, going on with the iteration these pieces become increasingly small, as long as they do not affect the flow anymore. In order to have an idea of the magnitude order of the disturbance which does not affect the flow, we can compute the base B_3 and the height H_3 of the most little triangle that make up the third iteration. The base scale every iteration with a factor equal to 1/3, therefore we have $B_3 = B_0/3^3$, where B_0 represent the base of the original triangle, which typically has a value of $100\mu m$ and therefore it is possible to obtain $B_3 \approx 4\mu m$. Eventually it is possible to compute the height exploiting its relation with the base $H_3 = B_3\sqrt{3}/6 \approx 1\mu m$. García-Mayoral et al. pointed out that riblet area is the most important parameter for the riblet effect evaluation, therefore it is even possible to conclude that a riblet cavity variation of about $4\mu m^2$ does not affect the viscous flow, and consequently the turbulent one. This is only a qualitative result, but it is important because reveals that the nanoscopic structure of the surface does not affect the flow and hence the drag reduction; therefore the surface can be machined until the nanoscopic dimension (it is important to underlie that the nanoscopic structure of the surface can be neglected for the fully wet case, but not for the superhydrophobic one as we will see in the last chapter).

The fractal riblets until now taken under consideration have been carried out through the addition of triangles with the vertex that point outward the wall; as the data shown, such a fractalization has a negative effect on the drag. It is now interesting to study the behavior of a fractal riblet constructed exploiting the same triangular mold but with each small triangle that point inward. The geometries obtained are sketched in figure 2.15.

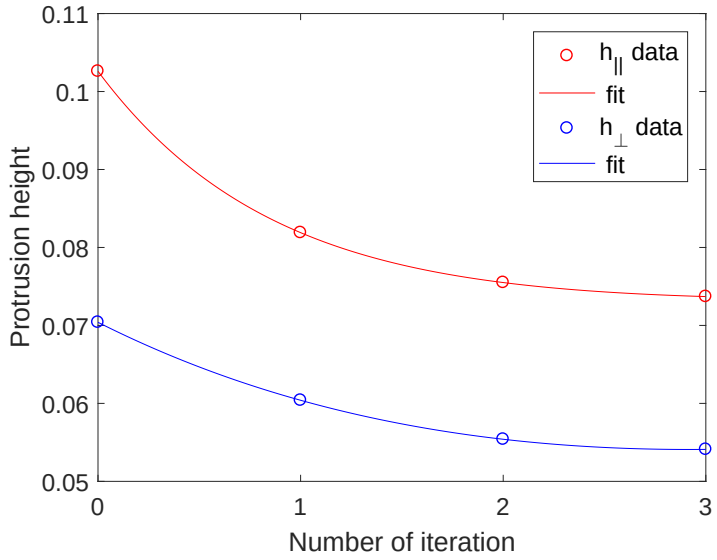

Figure 2.13: Parallel and perpendicular protrusion heights for the 120° triangle.

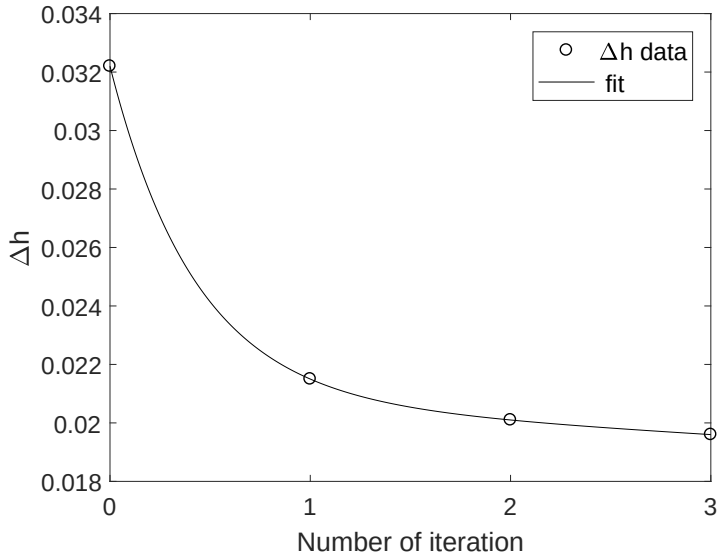

Figure 2.14: Difference between two protrusion heights for the 120° triangle.

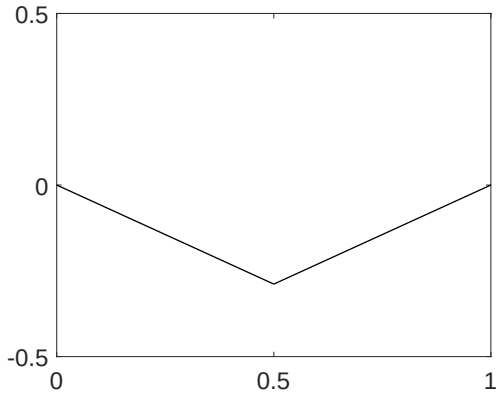

(a) 120° triangular mold.

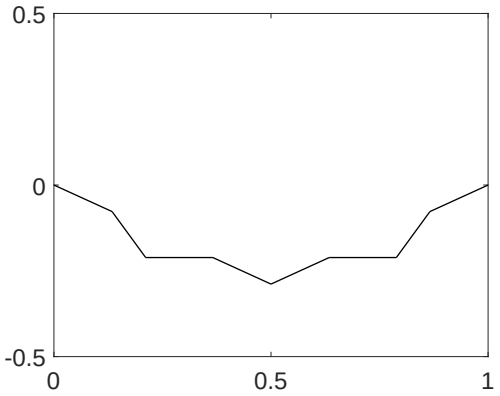

(b) First inward iteration of the 120° triangle.

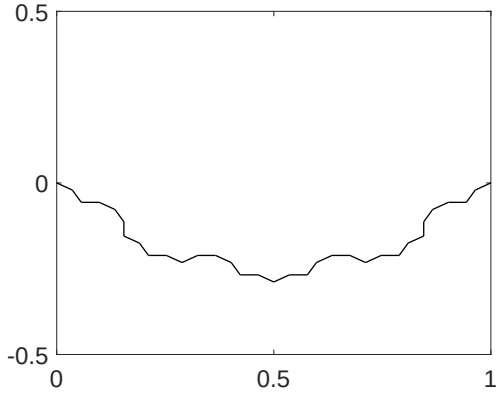

(c) Second inward iteration of the 120° triangle.

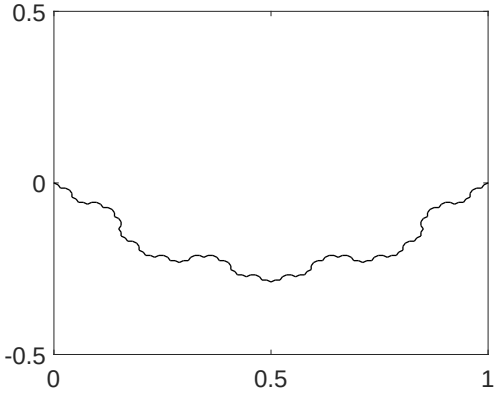

(d) Third inward iteration of the 120° triangle.

Figure 2.15: Riblet geometries with inward fractalization.

The results reported in table 2.3 reveals that each iteration generate an increment of all the protrusion heights; in figure 2.16 and figure 2.17 are shown their trends.

Iteration	$h_{\|\|}$	$h_{\perp}$	Δh
0	0.1026	0.0704	0.0322
1	0.1112	0.0715	0.0397
2	0.1138	0.0723	0.0415
3	0.1146	0.0725	0.0421

Table 2.3: Protrusion heights for all inward fractals iterations of the 120 ° triangle.

Comparing these exponential curves with figure 2.13 and figure 2.14, it stands out the change in the slope. We can therefore argue that the inward fractalized cavity affect

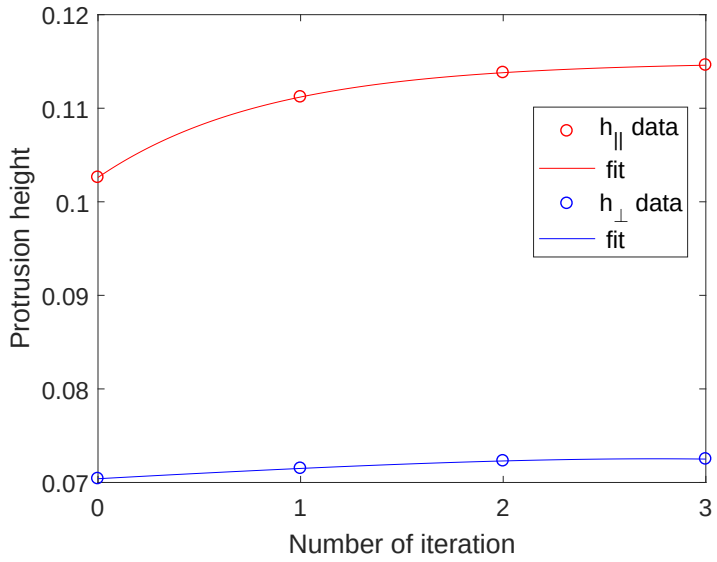

Figure 2.16: Parallel and perpendicular protrusion heights for inward fractals iterations of the 120° triangle.

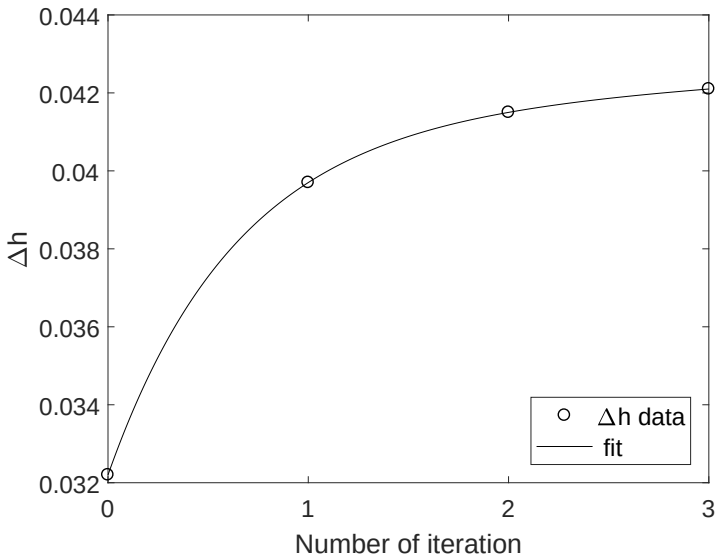

Figure 2.17: Difference between two protrusion heights for inward fractals iterations of the 120° triangle.

the viscous flow so that the drag reduction is increased. It emerges that the enhance of the cross-sectional riblet area (due to the outward fractalization) correspond to the increase of the drag reduction potential, whereas the reduction of the area (due to the inward fractalization) is related to the reduction of the drag reduction potential. The results is in agreement with that obtained by Garcia-Mayorcal [22], in which they indentify the cross-sectional area as the most important parameter in the riblet effectiveness evaluation. As well as the outward fractalization the protrusion heights approach a finite value, therefore we can observe again that a too small disturbance of the surface does not affect the protrusion heights and eventually the drag reduction. Another one difference between the two fractalization can be pointed out; though the fractalizations are symmetric respect to the original mold, the value obtained for the protrusion heights are not. Comparing the magnitude of the decrements of the protrusion heights obtained in the outward fractalization with the magnitude of the increment obtained in the inward fractalization, it can be noticed that the first one is larger then the second one. From this observation we can conclude that the viscous flow is more susceptible to the reduction of the riblet cavity rather then the increment of it; therefore the riblet effect can be easier reduced then increased. The wetted surface is equal in both the inward and outward fractalization, but the first one seems to promise a lower drag. It is therefore possible to argue in that case the existence of a mechanism which compensate the wetted wall surface.

The implemented boundary element code can even compute the velocity field inside the domain. The visualization of the velocity field contour allows to appreciate the effect of the riblet on the near wall flow. It is important to underlie that the BEM solves the Stokes equation, which does not present the convective term. Therefore, we are assuming that the convective term is negligible even away the wall, but such a simplification should be only valid near the wall, in the viscous sublayer. In consequence of this, the computed velocity fields must be used to evaluate the flow in the proximity of the wall. Such a limitation does not allow to understand the effect on the buffer and logarithmic layer as wall as the turbulent level, but it can be useful for the near wall flow structure understanding. The stream-wise velocity fields are shown in figure 2.18, figure 2.19 and figure 2.20. In all cases the gradient of the velocity on the peaks is different by that over the valleys, so that in the last region the low velocity zone

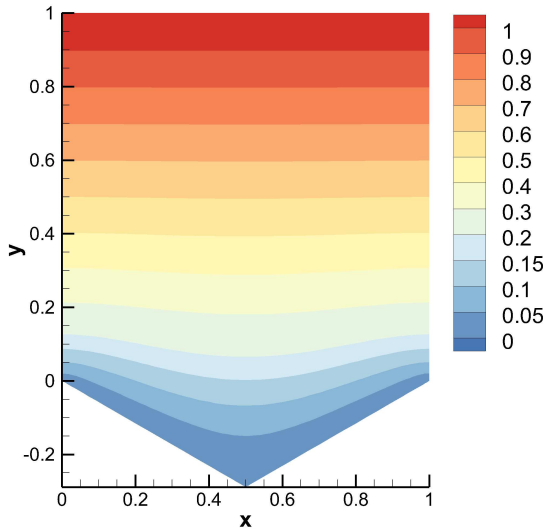

Figure 2.18: Stream-wise velocity field (w) for the simple 120° triangular riblet.

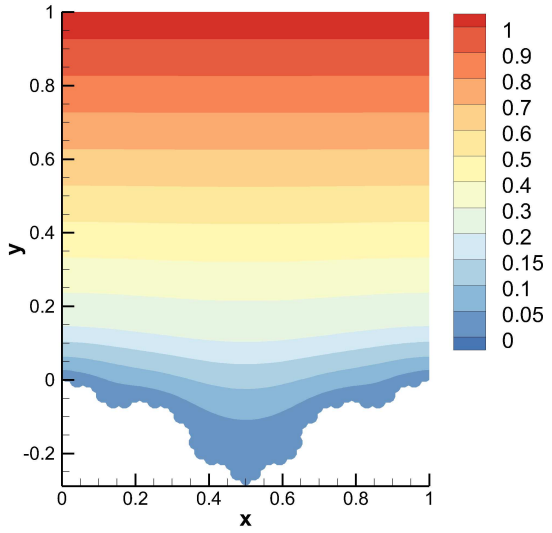

Figure 2.19: Stream-wise velocity field (w) for the third outward fractal iteration of the 120° triangular riblet.

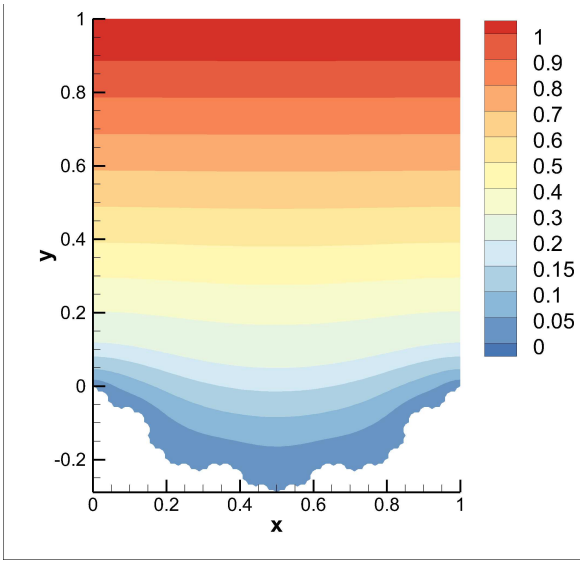

Figure 2.20: Stream-wise velocity field w for the third inward fractal iteration of the 120° triangular riblet.

is more width. This is a positive effect because keep the viscous flow away from the turbulent spots, which generate high velocity and hence high skin friction. Moreover, the high gradient on the peaks reveal the importance to have a perfect sharp (it reduce the surface where the high gradient is present).

In each case the black band lie on the bottom of the riblet cavity and it follow the boundary. Therefore the modification of the boundary shape even affect the black band shape.

In both the fractal riblet (figure 2.19 and figure 2.20) the geometry modification due to the first and second fractal iteration seems to affect the flow, because the low velocity region (represented by the band attached to the riblet bottom) is modified. The third fractal iteration does not affect the flow (as already seen thank to the protrusion heights). In the outward fractalization the black band is shifted up and this make for a lower longitudinal protrusion height. On the contrary the inward fractalization shift down the black band. In figure 2.21, figure 2.22 and figure 2.23 are reported the y-velocity component contour and the stream-lines in the z-y plane. The transverse flow over the riblet is sustained by the imposed linear velocity, which animate the flow from the left to the right of the domain. Such a imposition generate a down-wash of the normal velocity on the left riblet tip, and an up-wash on the right one. This effect change the stream-lines path, and force them to the bottom of the riblet.

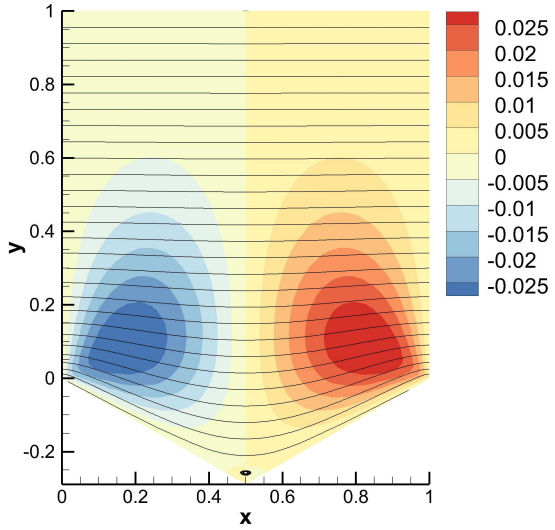

Figure 2.21: Span-wise velocity field (v) and streamlines for the simple 120° triangular riblet.

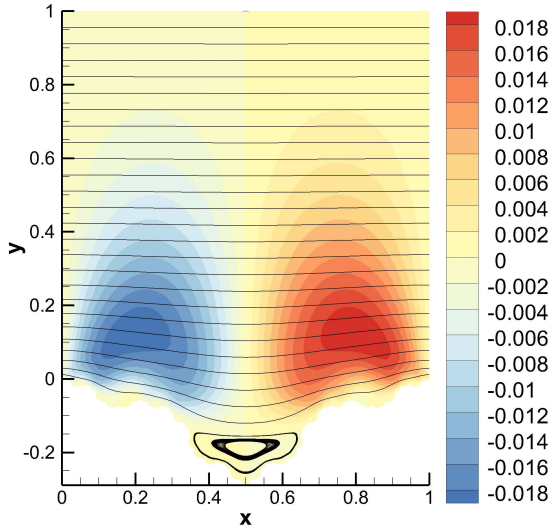

Figure 2.22: Span-wise velocity field (v) nad streamlines for the third outward fractal iteration of the 120° triangular riblet.

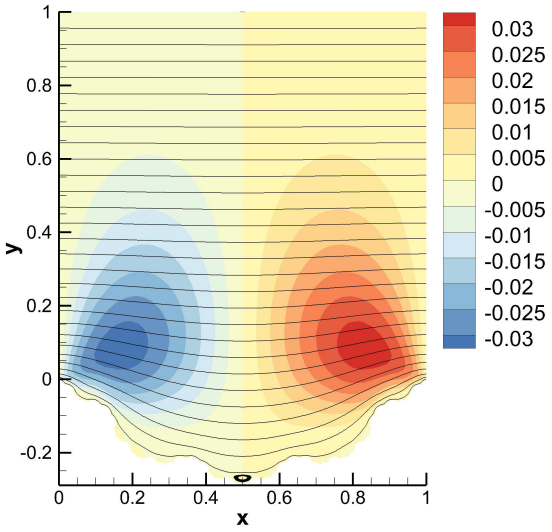

Figure 2.23: Span-wise velocity field (v) and streamlines for the third inward fractal iteration of the 120° triangular riblet.

The v component of the velocity bring down even the stream-wise component, and contribute to hold the flow in the riblet cavity. The inward fractal riblet generate the highest normal velocity magnitude, so that it is better capable to hold down the flow in the riblet cavity, and this can may be associated with the higher drag reduction. The stream-lines on the riblet bottom reveal in all three cases a corner eddy (Moffatt et al. [19]) with various dimension. The outward fractal riblet present the biggest vortex, and it can may be related to the bad drag reduction performances.

2.7.3 90° triangle

In order to study the period on depth ration effect, another triangular riblet shape has been studied (figure 2.24a). It has the angle to the vertex of 90° ($L/H = 0.5$) instead of 120° ($L/H = 0.29$), therefore, since the period must be equal to one in both cases (as explained in section 2.7.1), the new geometry is deeper, and consequently it has an higher cross-sectional area.

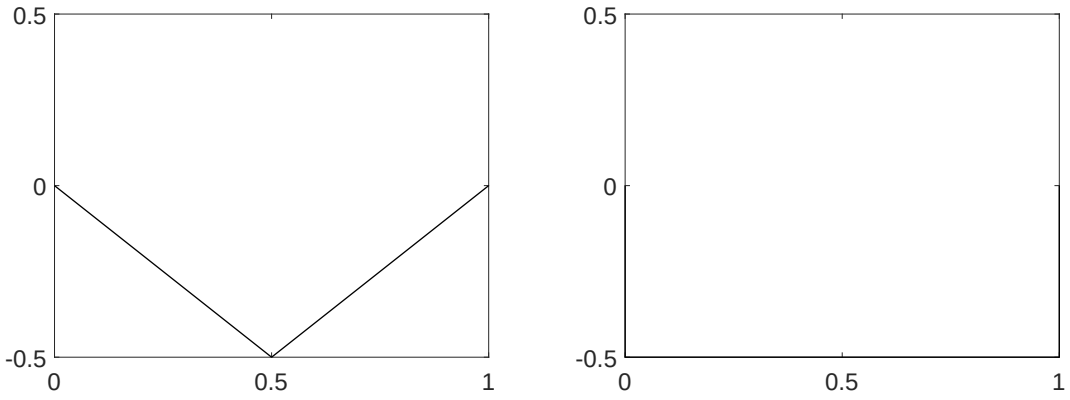

(a) Triangular riblet. *(b)* Blade riblet.

Figure 2.24: Geometries under investigation.

Since riblet effect depends on (but not only) the cross-sectional area of the wall cavity, it is reasonable to suppose that the drag reduction will be higher then that obtained for the 120° triangle. The data reported in table 2.4 show the value of Δh; it is higher than that found for the previous shape, and this means a better drag reduction as argued with the consideration about the riblet area.

Case	$h_{\|\|}$	$h_{\perp}$	Δh
Blade riblet	0.207	0.0834	0.1236
Triangular riblet	0.1396	0.0788	0.0608

Table 2.4: Comparison between rectangular and triangular riblet.

All the 90° fractal iteration are shown in figure 2.11, and the computed protrusion

heights are reported in table 2.5, whereas their trend are sketched in figure 2.25 and figure 2.26.

Iteration	$h_{\|\|}$	$h_{\perp}$	Δh
0	0.1396	0.0788	0.0608
1	0.1117	0.0744	0.0373
2	0.0989	0.068	0.0309
3	0.0949	0.0659	0.029

Table 2.5: Protrusion heights for all the fractals iterations of the 90° triangle.

It can be immediately understood the similarity with the 120° triangular case. The protrusion heights decrease rapidly going on with the iteration and approach a finite value. Again it is possible to confirm that a small disturbance does not affect the protrusion heights and the drag reduction. Another similarity can be found in the Δh value of the original mold and that of the first iteration; both are affected by the biggest decrease. The decrease magnitude is slightly different (it is bigger for the 120° case), because the 90° triangular mold brings to a stronger reduction of the cavity.

As with as the 120° triangle, an inward fractalization has been constructed. The shapes obtained are sketched in figure 2.27.

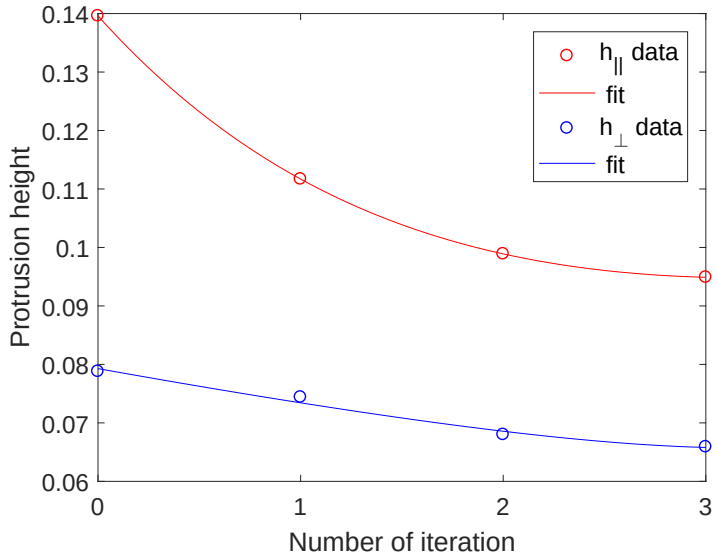

Figure 2.25: Parallel and perpendicular protrusion heights for the 90° triangle.

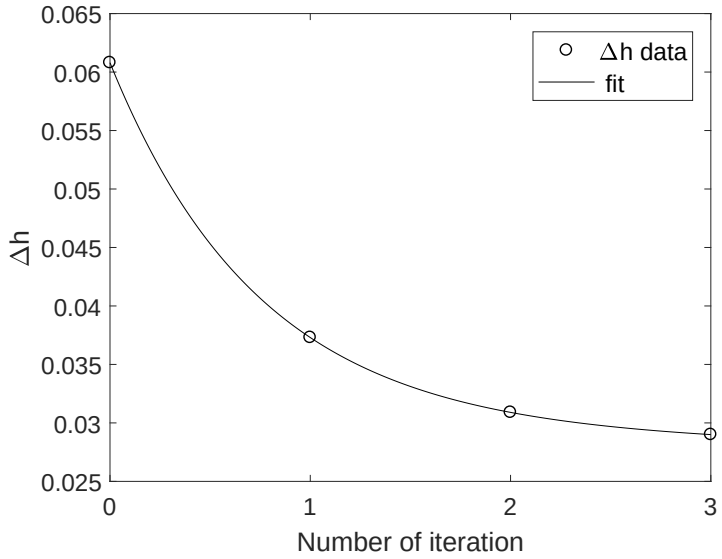

Figure 2.26: Difference between two protrusion heights for the 90° triangle.

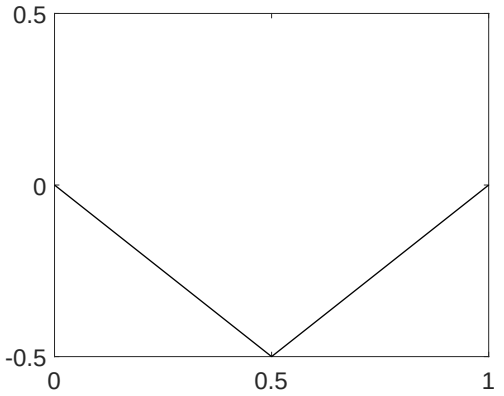

(a) 90° triangular mold.

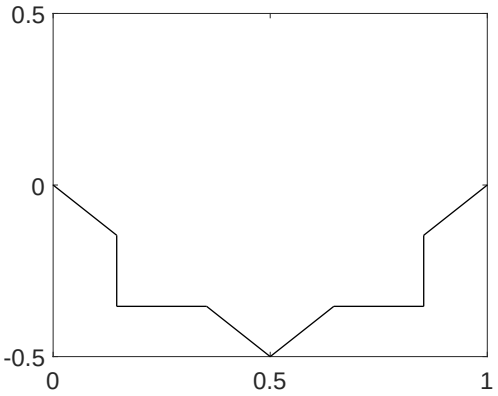

(b) First iteration for the 90° triangle.

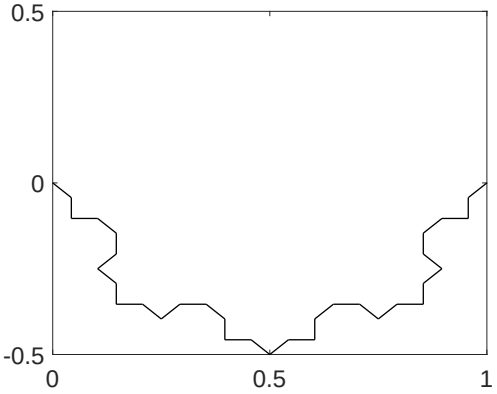

(c) Second iteration for the 90° triangle.

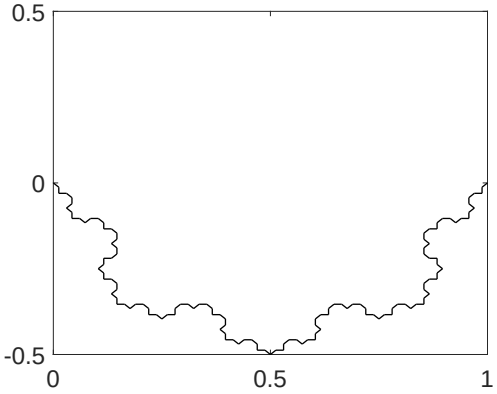

(d) Third iteration for the 90° triangle.

Figure 2.27: Constructed inward fractals geometries.

Even in this case the data reported in table 2.6 and shown in figure 2.28 and figure 2.29 confirms the previous results.

Iteration	$h_{\|\|}$	$h_{\perp}$	Δh
0	0.1396	0.0788	0.0608
1	0.1464	0.0779	0.0685
2	0.1495	0.0782	0.0713
3	0.1506	0.0783	0.0723

Table 2.6: Protrusion heights for all inward fractals iterations of the 90° triangle.

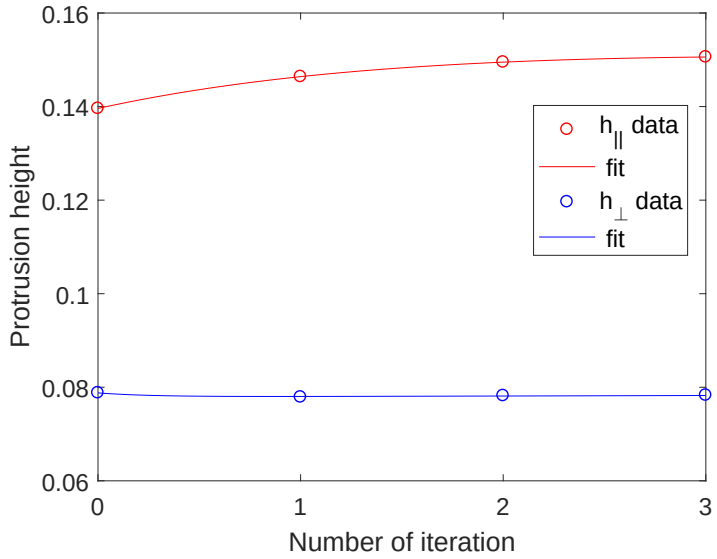

Figure 2.28: Parallel and perpendicular protrusion heights for inward fractals iterations for the 90° triangle.

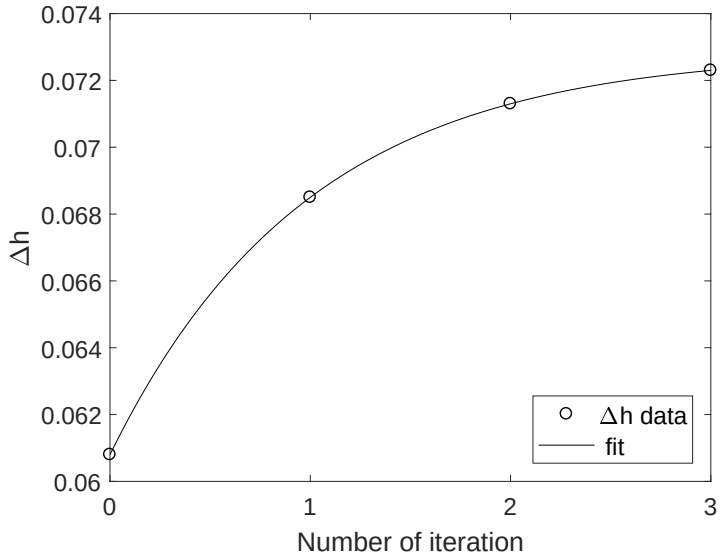

Figure 2.29: Difference between two protrusion heights for inward fractals iterations for the 90° triangle.

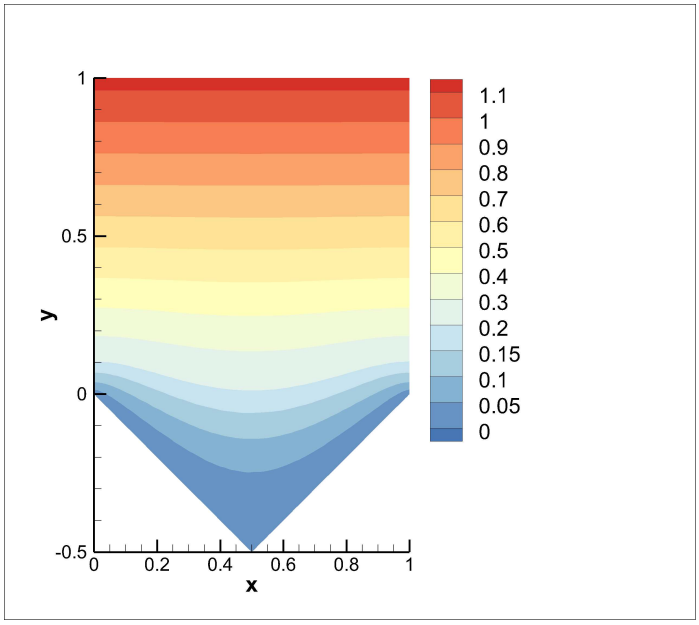

Figure 2.30: Stream-wise velocity field for the simple 90° triangular riblet.

The velocity fields have been computed. The stream-wise velocity is shown in figure 2.30, figure 2.31 and figure 2.32. Comparing the 90° flow fields with that obtained in the paragraph, it is possible to point out some differences. The velocity gradient on the valley is smaller, and this reduces viscous skin friction. The effect is due to the enhance of the riblet cavity, that allow a deeper penetration of the flow. The low velocity zone is wider, so it is possible to suppose that the high velocity spots due to the turbulence are dumped in a better way. The normal velocity contour, shown in figure 2.33, figure 2.34 and figure 2.35, reveal a bigger corner eddy in all the cases.

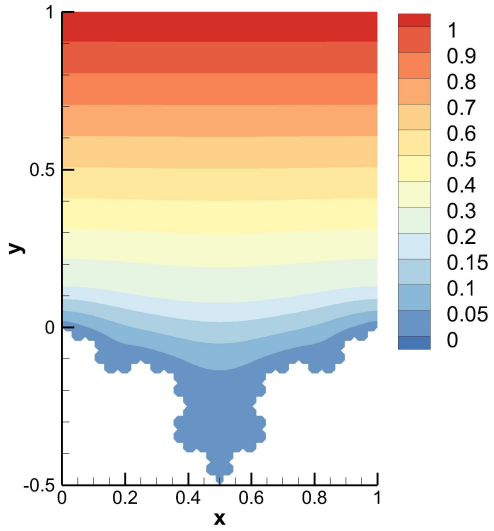

Figure 2.31: Stream-wise velocity field for the third outward fractal iteration of the 90° triangular riblet.

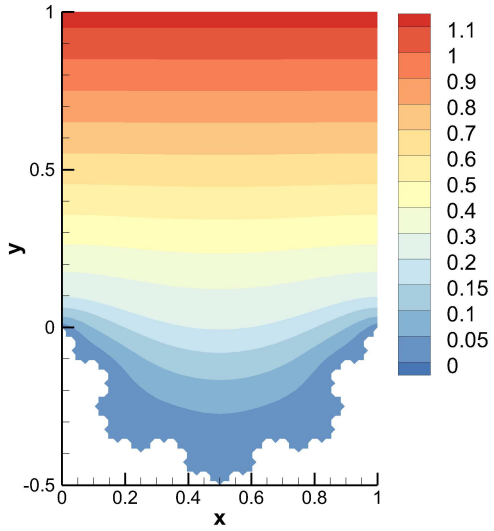

Figure 2.32: Stream-wise velocity field for the third inward fractal iteration of the 90° triangular riblet.

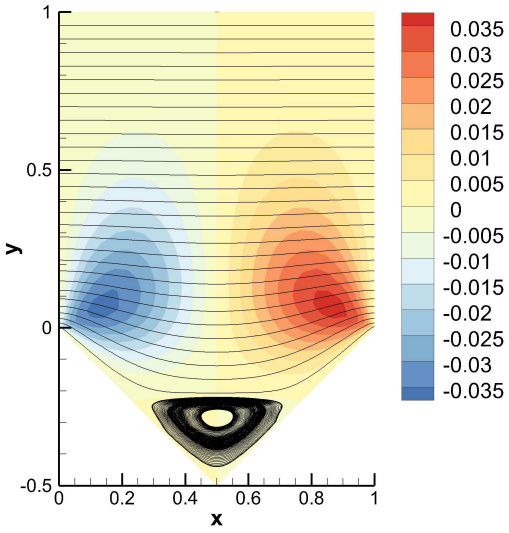

Figure 2.33: y velocity component field for the simple 90° triangular riblet.

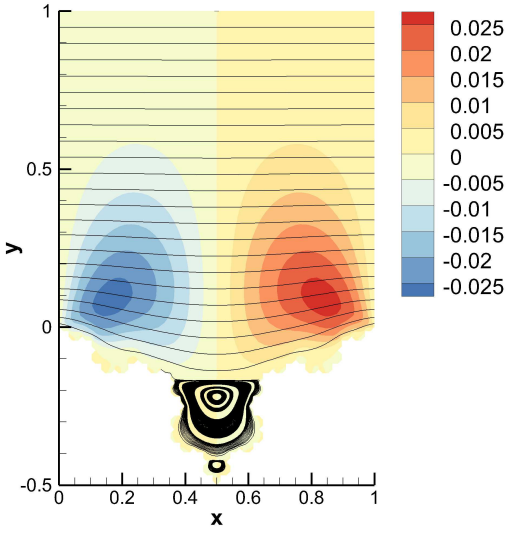

Figure 2.34: y velocity component field for the third outward fractal iteration of the 90° triangular riblet.

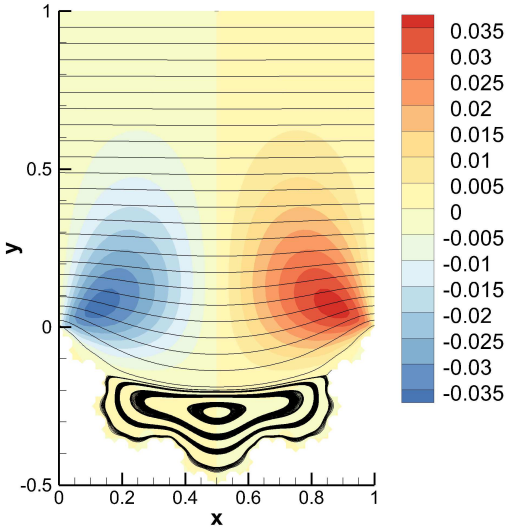

Figure 2.35: y velocity component field for the third inward fractal iteration of the 90° triangular riblet.

Chapter 3

Macroscopic problem

3.1 Numerical method

The macroscopic problem represent the second part of this work. It aim at carrying out the drag over a fractal riblet plates, and compare it with that obtained with simple triangular riblets. To do so, a rectangular channel is studied through direct numerical simulation.

3.1.1 Finite volume method

The Finite Volume Method (FVM) is a discretization approach in which the solution domain is subdivided into a finite number of contiguous Control Volumes (CVs), and the N-S equations are applied to each CV. At the centroid of each CV lays a computational node at which the variables values are to be evaluated. Before proceeding to the mathematical description of the method, we show the equations 3.1, that are the dimensionless continuity and momentum equations herein used to perform the direct numerical simulation.

$$\begin{cases} \dfrac{\partial u_i}{\partial x_i} = 0 \\ \\ \dfrac{\partial u_i}{\partial t} + u_j \dfrac{\partial u_i}{\partial x_j} = -\dfrac{\partial p}{\partial x_j} + \dfrac{1}{Re} \dfrac{\partial^2 u_i}{\partial x_j \partial x_j} + f_i. \end{cases} \tag{3.1}$$

The variables used to yields dimensionless equations 3.1 are δ and u_τ. The first one represents the half width of the channel in the y direction, whereas the second is the shear velocity defined as $u_\tau = \sqrt{\tau_{wall}/\rho}$. Re denotes the Reynolds number defined as $Re = U_0 \delta / \nu$.

The first step of the method deals with the integration of this dimensionless N-S equations over a single control volume called Ω. We use a Cartesian grid and a collocated arrangement, therefore all the variable are calculated in the cell center. In figure 3.1 is shown a three-dimensional Cartesian control volume together with the notation used. The CV consist of six plane faces, denoted with lower case letters (e,w,n,s,t,b) corresponding to their orientation with respect to the central node P.

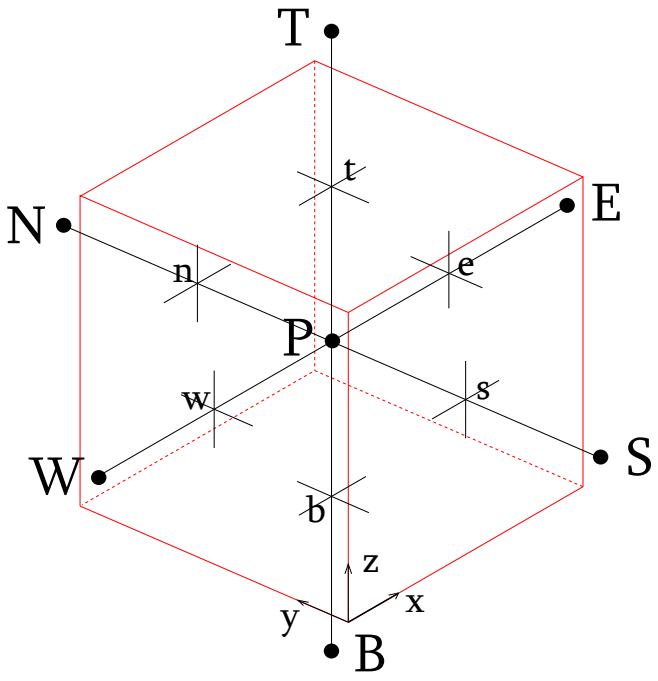

Figure 3.1: Three dimensional control volume for a Cartesian grid.

Once the integration on the control volume 3.1 is performed, the method exploits the Gauss's theorem (and the incompressibility condition for the diffusive term) to do the following transformations:

- The continuity equation became

$$\int \nabla \cdot \mathbf{u} \mathrm{d}\Omega = \int_S \mathbf{u} \cdot \mathbf{n} \mathrm{d}S = 0 \tag{3.2}$$

- The convective term of the momentum equation become

$$\int_\Omega u_j \frac{\partial u_i}{\partial x_j} \mathrm{d}\Omega = \int_S u_i \mathbf{u} \cdot \mathbf{n} \mathrm{d}S \tag{3.3}$$

- The diffusive term of the momentum equation become

$$\int_\Omega \frac{1}{Re} \frac{\partial^2 u_i}{\partial x_j \partial x_j} \mathrm{d}\Omega = \int_S \frac{1}{Re} \nabla u_i \cdot \mathbf{n} \mathrm{d}S \tag{3.4}$$

After the integration and the application of above transformation, the N-S equations

read

$$\begin{cases} \int_S \mathbf{u}\cdot\mathbf{n}\mathrm{d}S = 0 \\ \\ \int_\Omega \frac{\partial u_i}{\partial t}\mathrm{d}\Omega + \int_S u_i\mathbf{u}\cdot\mathbf{n}\mathrm{d}S = -\int_\Omega \frac{\partial p}{\partial x_j}\mathrm{d}\Omega + \int_S \frac{1}{Re}\nabla u_i\cdot\mathbf{n} + \int_\Omega f_i\mathrm{d}\Omega. \end{cases} \tag{3.5}$$

The equation 3.5 presents integrals performed on the CV's surface S or on the volume Ω, and both must be approximated. For the first type, we can call the generic quantity that flows through the surface as ϕ and thanks to the linearity of the integral we can write

$$\int_S \phi\mathrm{d}S = \sum_{k=1}^{6}\int_{S_k}\phi\mathrm{d}S, \tag{3.6}$$

where 6 is the number of control volume faces and ϕ can be both the convective or diffusive flux. Equation 3.6 is still exact, but we need now to introduce the first approximation. The surface integral of ϕ, for an arbitrary face k is estimated with the mid-point rule, that is the integral on the square surface is approximated with the following:

$$\int_{S_k}\phi\mathrm{d}S \approx \phi_k S_k, \tag{3.7}$$

where S_k is the area of the k-th square face of the cube, and ϕ_k is the value of ϕ at the center of the square face. It is possible to show that this approximation is of second order accuracy. Whereas S_k is a geometrical information and it can be easily computed, ϕ_k contains the unknowns that we want to determine. Moreover, since ϕ_k is taken on the square face center, the unknowns inside it are too, therefore we must express ϕ_k in terms of the nodal value. To do so, we can do an interpolation between two numerical nodes; for example, if we want to determine the value of ϕ_k on the east side, we do the interpolation between the P node and the E node. Hence, referring to the figure 3.1, the value of ϕ at CV-face center is obtain by linear interpolation between the two nearest nodes, as follows (e.g e face):

$$\phi_e = \lambda\phi_P + (1-\lambda)\phi_E, \qquad \lambda = \frac{x_e - x_E}{x_E - x_P}. \tag{3.8}$$

This scheme is called central difference scheme (CDS) and it is of second order accuracy.

For clarity, the discretization of the convective fluxes will be shown only for the e-face of the Cartesian CV shown in figure 3.1 and only for the first component of the velocity vector. The fluxes at the other surfaces can be treated in the same fashion applying the appropriate subscripts permutation. Before to apply the above approximation we have to explain the particular treatment of the non-linear convective term; inside it the velocity unknown appear two times, and in order to avoid problems, we compute the term $\mathbf{u} \cdot \mathbf{n}$ with the value at the previous time-step. Doing so, $\mathbf{u} \cdot \mathbf{n}$ is a constant and it can drop the integral. The discrete convective flux read:

$$\int_{S_e} u_i \mathbf{u} \cdot \mathbf{n} \mathrm{d}S = \mathbf{u} \cdot \mathbf{n} \int_{S_e} u_i \mathrm{d}S \approx \mathbf{u} \cdot \mathbf{n} \int_S \left[\lambda \phi_P + (1-\lambda)\phi_E\right] \mathrm{d}S =$$

$$= \mathbf{u} \cdot \mathbf{n} \int_S \mathrm{d}S \left[\lambda \phi_P + (1-\lambda)\phi_E\right] = \dot{m}_e \left[\lambda \phi_P + (1-\lambda)\phi_E\right], \tag{3.9}$$

and the diffusive one

$$\int_S \frac{1}{Re} \nabla u_i \cdot \mathbf{n} \mathrm{d}S \approx \frac{S(u_E - u_P)}{Re(x_E - x_P)} \tag{3.10}$$

$\dot{m}_e = \mathbf{u} \cdot \mathbf{n} \int_S \mathrm{d}S$ is the mass flow rate through the surface e. The spatial discretization is completed by the approximation of pressure gradient and body forces, also called source terms. For an arbitrary source term q the following approximation is applied:

$$\int_\Omega \mathbf{q} \mathrm{d}\Omega = \Delta\Omega \mathbf{q}_P \tag{3.11}$$

The integral is estimated by the product between the central value of $\mathbf{q}$ in the control volume center and the cell volume. This is again a second order accurate approximation. After the space discretization, a time advancement strategy is necessary, and we will analyze the method herein adopted in the next section.

3.1.2 Fractional step

The fractional step method is a technique to advance in time the fluid flow governing equations and was firstly developed by Chorin [6] and then improved by other authors. The algorithm is based on Helmholtz–Hodge decomposition or simply Hodge decomposition; it states that the vector field $\mathbf{u}$ defined on a simply connected domain can

be uniquely decomposed into a divergence-free (solenoidal) part and an irrotational part. Typically, the algorithm consists of two stages: prediction and correction. In the prediction step, the momentum equation is solved without the pressure terms, but the resulting velocities does not satisfy the continuity equation. In the correction step the previous solution is corrected and the velocity field is projected onto a divergence-free field. Several numerical implementation are available in the literature,and we will present the fractional step version proposed by Kim and Moin [11]. The method is semi-implicit and not all the terms of the momentum equation are discretized in time in the same manner. In particular the second order Crank-Nicolson scheme is used for the wall-normal diffusive term and the second order Adams-Bashforth scheme for all of the other terms in momentum equation. The first step of the method aim at solving the following equation

$$\frac{\hat{u}_i - u_i^n}{\Delta t} = C(u_i^n, u_i^{n-1}) + \frac{1}{Re} D(\hat{u}_i, u_i^n) + \frac{\delta p}{\delta x}, \tag{3.12}$$

where C and D represent respectively the discretization of the convective and diffusive terms. In the predictor step we solve the system of equations 3.12 for $\hat{u}_i$, but it will not satisfy the continuity equation. Therefore, the field $\hat{u}_i$ has to be projected onto a divergence-free field u_i^{n+1} and to do so we employ the so called projection step that follows. We write the complete discretized N-S equation

$$\frac{u_i^{n+1} - u_i^n}{\Delta t} = C(u_i^n, u_i^{n-1}) + \frac{1}{Re} D(\hat{u}_i, u_i^n) - \frac{\delta p}{\delta x_i} \tag{3.13}$$

and we substitute the sum of the convective and diffusive terms with the equation 3.12

$$\frac{u_i^{n+1} - \hat{u}_i}{\Delta t} = -\frac{\delta p}{\delta x_i} \tag{3.14}$$

Taking the divergence of the equation 3.14

$$\frac{\delta}{\delta x_i}\frac{\delta p}{\delta x_i} = \frac{1}{\Delta t}\frac{\delta \hat{u}_i}{\delta x_i} \tag{3.15}$$

we obtain the Poisson equation for the pressure-like variable, from which we can compute ϕ, and afterwards we can find the velocity field u_i^{n+1} solving the equation 3.14.

3.2 Computational domain and grid spacing

The flow geometry and the coordinate system are shown in figure 3.2. The arrow show the flow direction, and the upper and the lower plates represent the wall, therefore the no slip condition is here applied.

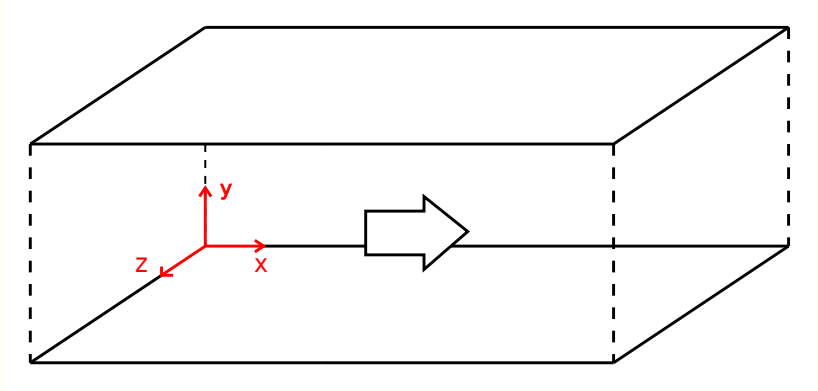

Figure 3.2: Geometry taken under consideration for the direct numerical simulation.

In the streamwise and spanwise direction the periodic boundary condition is used. The aforementioned condition can be justified if the computational box (period) is chosen to include the largest eddies in the flow. In order to choose a sufficiently larger domain, we examine the experimental two-point correlation measurements used in Kim et al. [12] and shown in figure 3.3 and figure 3.4.

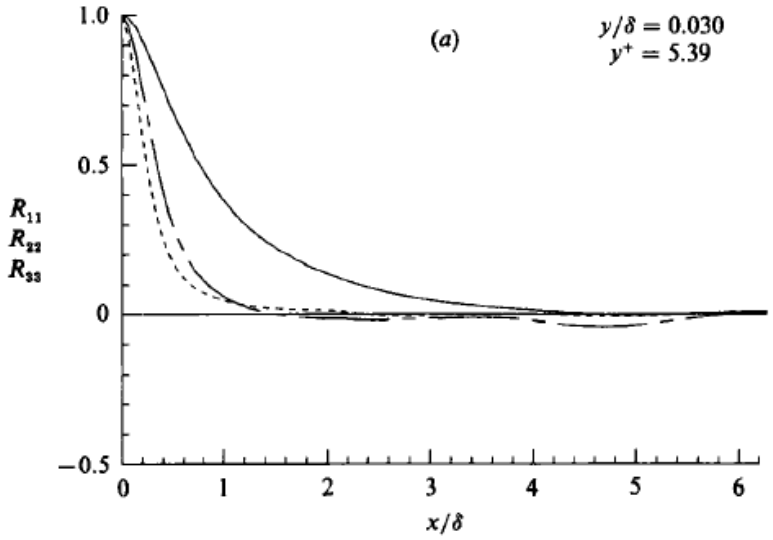

Figure 3.3: Two-points correlation of the velocity vector along the stream-wise direction.

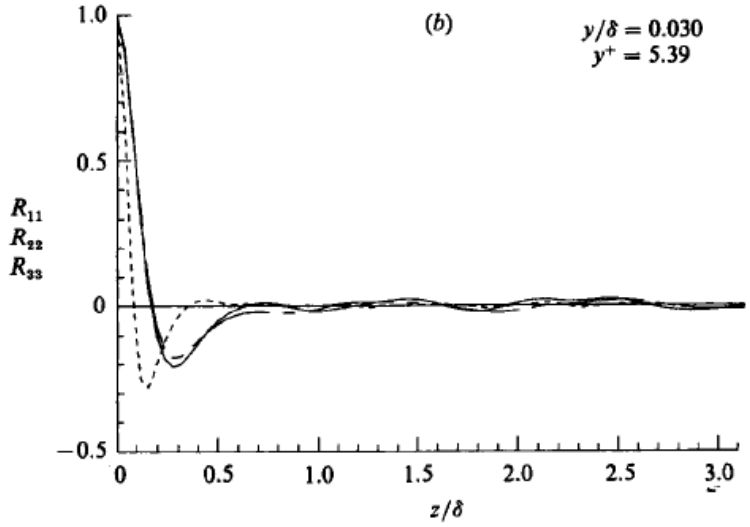

Figure 3.4: Two-points correlation of the velocity vector along the span-wise direction.

Looking at these correlations, it has been established the channel dimension as 2π x π in dimensionless unit, thereby the end of the channel in the periodic direction lay where the correlation of the velocities is almost zero. Therefore the domain enclose the largest eddies in the flow, and the integral scale is taken into account. In terms of unit wall the domain is $1106 \times 352 \times 552$ [1]. The computation is carried out with a resolution of grid points $161 \times 201 \times 129$ (more then 4 million points) for a Reynolds number of 2800, which is based on the bulk velocity, and the channel half-width δ (a Reynolds number of 176 based on the wall shear velocity u_τ). With this grid, the spacing in the streamwise and spanwise directions are respectively $\Delta x^+ = 7$ u.w. and $\Delta z^+ = 4$ u.w.. Moreover, a non-uniform mesh is used in the normal direction; it is stretched through a hyperbolic tangent function and the first point near the wall is located at $y^+_{min} = 0.052$. Such a grid is sufficiently fine to solve the essential turbulent scale, and no subgrid model is used.

[1] The channel can be considered sufficiently large even because of the length of it in each direction are higher then the minimal channel lengths [13].

3.3 Navier boundary conditions

Until now, we have described the methods used to implement the direct numerical simulation, but we have not yet introduced the boundary conditions; this is a fundamental point because allow us to take into account the triangular riblet wall and its fractalizaition in a simple way. In fact, the groove of the riblet surface are extremely small, and the grid used to study it should be too fine and complex, therefore we cannot take into account such a geometry. In order to avoid the problem, we simulate the riblet plate through the application of the Navier boundary conditions 3.16 (in both the stream- and span-wise direction), in which the slip lengths coincide with the protrusion heights. In figure 3.5 are sketched the velocity profile from which the slip lengths arise.

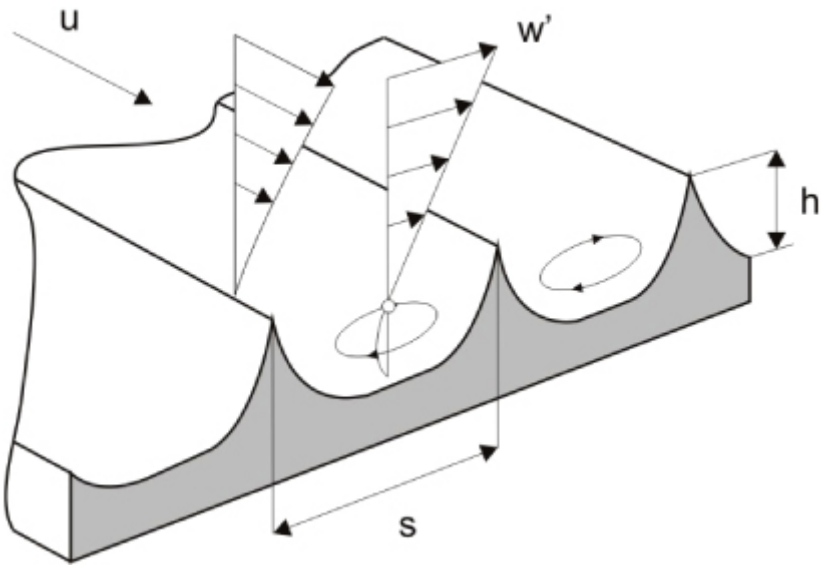

Figure 3.5: Velocity profile from which the protrusion heights are computed.

This particular condition can be simulated applying the two slip boundary condition 3.16

$$u_{\text{wall}} = kh_{||} \left.\frac{\partial u}{\partial y}\right|_{\text{wall}} \qquad w_{\text{wall}} = kh_{\perp} \left.\frac{\partial w}{\partial y}\right|_{\text{wall}} \tag{3.16}$$

where u_{wall} and w_{wall} are respectively the stream-wise and span-wise velocities at the wall (their value is non-zero), k is a scale coefficient, $h_{||}$ and $h_{\perp}$ are respectively the parallel and the perpendicular protrusion heights and $\partial u/\partial y$ and $\partial w/\partial y$ are the derivatives of the velocities computed on the wall. The k coefficient is needed because the quantities used to yields dimensionless the Stokes equation (the governing equation of

the microscopic problem from which we carried out the protrusion heights) are different from that used for the Navier-Stokes equations solved in the DNS. Therefore we cannot directly give in input the value carried out with the boundary element method, but we must adjust it so that it results adimensionalized through the half channel width δ as follow

$$\frac{h_{||}}{\delta} = \frac{b}{\delta} h_{||}^{BEM} = k h_{||}^{BEM}, \qquad k = \frac{b}{\delta} \tag{3.17}$$

where b indicate the riblet spacing, $h_{||}$ and $h_{||}^{BEM}$ represent respectively the dimensional longitudinal protrusion height and that computed with the BEM. The value of k must be fixed, and once it has been chosen, the dimensions of the riblet period respect to the channel has been fixed. We have chosen $k = 0.05$, which corresponds to a $b^+ = 10$.

The boundary conditions 3.16 assign a non-zero value to the streamwise and spanwise velocities at the wall. The effect of these two boundary condition has been studied by T. Min and J. Kim [24]; they have taken under consideration three different cases: only streamwise slip boundary condition, only spanwise slip condition and both the condition together. As expected in the first case the drag reduction was obtained, whereas in the second case, when the slip-boundary condition is used in the spanwise direction, the mean drag increases. The physical reason behind the last behavior is that the longitudinal vortex are dumped with a no slip condition, and are less dumped with a slip condition, so that the turbulent oscillation are free to develop. Regarding the last case, there is a balance between the reduction of the drag due to the streamwise slip condition and the increase of it due to the slip spanwise condition so that the effect of the riblet is reproduced.

Eventually we must empathize that this kind of approach in the study of the riblet has never been tested and validated, hence the results should be confirmed through experiment. Nevertheless this method seems to be correct from a conceptual point of view, in fact the effect of the spanwise slip boundary condition on the flow is similar to that performed by the riblet, both act on the cross flow.

3.4 Validation of the code

In order to validate the code implemented for the DNS, we have taken as reference the study performed by Kim, Moin and Moser in 1986 [12] at the NASA Ames Research Center, in which they carried out one of the first direct numerical simulation of a turbulent channel flow. They chose a $4\pi\delta \times 2\delta \times 2\pi\delta$ channel, where δ is the channel half width in the y-direction. They numerically solved the unsteady Navier-Stokes equations with a Reynolds number of 2800, based on the bulk velocity and the channel half-width δ (a Reynolds number of 180 based on the wall shear velocity u_τ), with a grid resolution of $192 \times 129 \times 160$ in x, y, z. With this grid, the spacing in the stream-wise and span-wise directions are respectively $\Delta x^+ = 12$ u.w. and $\Delta z^+ = 7$ u.w.. Moreover, a non-uniform mesh is used in the normal direction, and the first mesh point away from the wall is at $y^+ = 0.05$. Doing so they solved all essential turbulence scales on the computational grid and no subgrid model was used. Moreover, they computed a large number of turbulence statistics that are even now in agreement with the experimental data.

The case solved in the present work have some differences respect to the Kim and Moin case: the grid herein used is finer then Kim and Moin one and the method used to solve the equations is different [2]. In order to validate the dns code, we have carried out the velocity root mean square in each direction and we have compared them with that obtained by Kim and Moin, as presented in figure 3.6, 3.7 and 3.8

[2] In [12] a spectral code was employed.

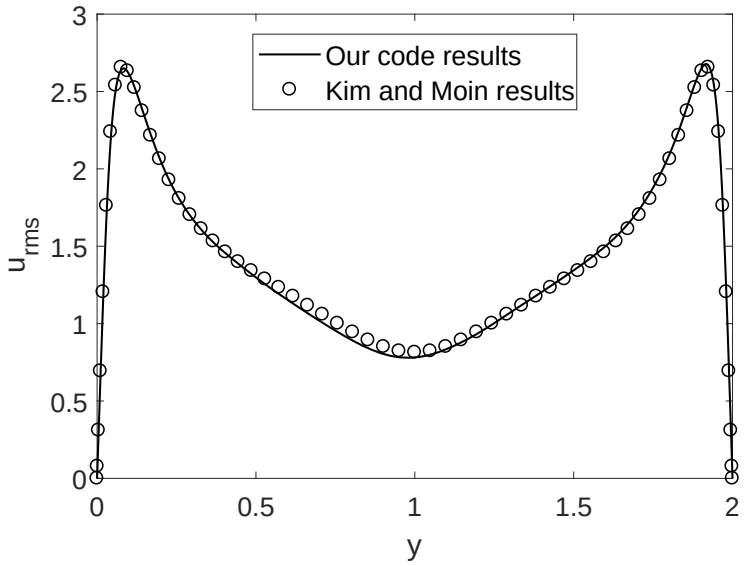

Figure 3.6: Root mean square of the stream-wise velocity u' fluctuation.

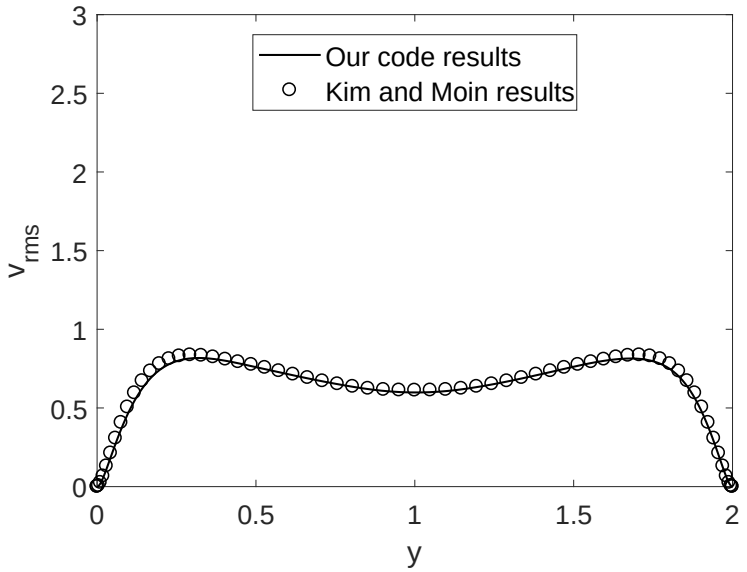

Figure 3.7: Root mean square of the normal velocity v' fluctuation.

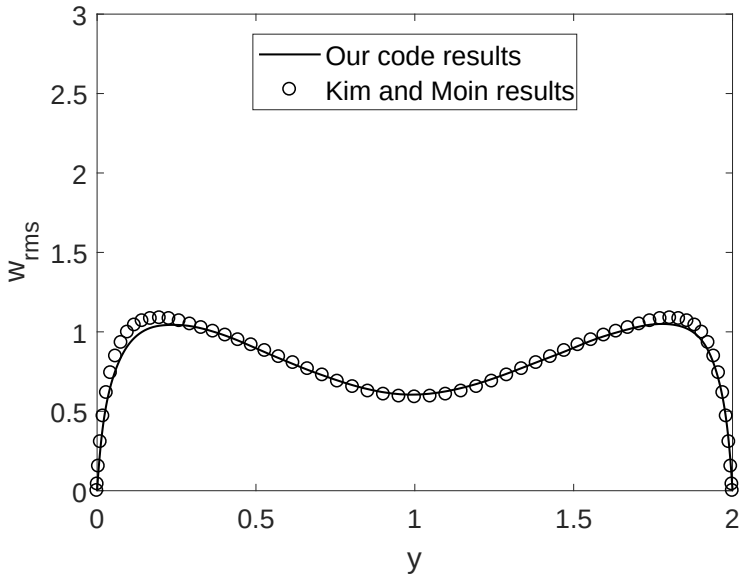

Figure 3.8: Root mean square of the spanwise velocity w' fluctuation.

The figures show a very satisfying agreement of the results.

3.5 Results

In order to perform the direct numerical simulations, we have taken under consideration the 90° triangular riblet and its third inward fractalzation, both sketched in figure 2.27. Luchini's theory relate an high value of Δh to an high drag reduction; since the 90° show an higher Δh then the 120° riblet, it seems to be the more promising geometries in terms of drag reduction. Therefore we have chosen it. Moreover, this shape show the highest increase of the Δh value when the fractalization procedure is applied. This is an important feature, because the fractalization modify the riblet geometry on the scale of nanometers, hence we can suppose to have small variation of the flow. Therefore, higher is the change in the Δh and better we can appreciate the changing in the flow. We have only studied the third iteration because it represent the limit at which the protrusion height do not vary anymore. In table 3.1 are shown the value of the protrusion heights for the selected cases.

Iteration	$h_{\|\|}$	$h_{\perp}$	Δh
0	0.1396	0.0788	0.0608
3	0.1506	0.0783	0.0723

Table 3.1: Protrusion heights for the 90° triangular riblet and for its third fractalization.

In this section the DNS results are shown and commented. Three different channels have been studied: the completely smooth channel (the same used for the validation), the channel with simple 90° triangular riblet and the channel with the third fractal iteration for the 90° riblet. It is worth to remember that the lower plates of the riblet channels is the one with the grooved wall. The results obtained are reported in table 3.2.

Case	Re	$\lvert\partial p/\partial x\rvert$	u_τ	τ_{wall}	Re_τ	DR
Smooth	2777	0.00397	0.0634	0.0040	177	–
Triangular tiblet	2777	0.00376	0.0613	0.0038	170.4	5.3%
Fractal riblet	2777	0.00370	0.0608	0.037	168.9	6.8%

Table 3.2: Results obtained from the DNS simulation. Re is the Reynolds number based on the bulk velocity, $\partial p/\partial x$ is th mean pressure gradient, u_τ is the friction velocity, τ_{wall} is the skin friction, Re_τ is the Reynolds number based on the friction velocity, DR is the drag reduction percentage.

The first parameter taken under consideration is the pressure gradient between the outlet and the inlet. It is fundamental because allow us to compute the drag applied by the flow on the plates of the channel. It is worth to underlie that the code computes the value of the pressure gradient every iteration, and it aim at maintaining the bulk velocity, computed as shown in equation 3.18, equal to one.

$$U_m = \frac{1}{2}\int_0^2 \bar{u}\mathrm{d}(y/\delta) \tag{3.18}$$

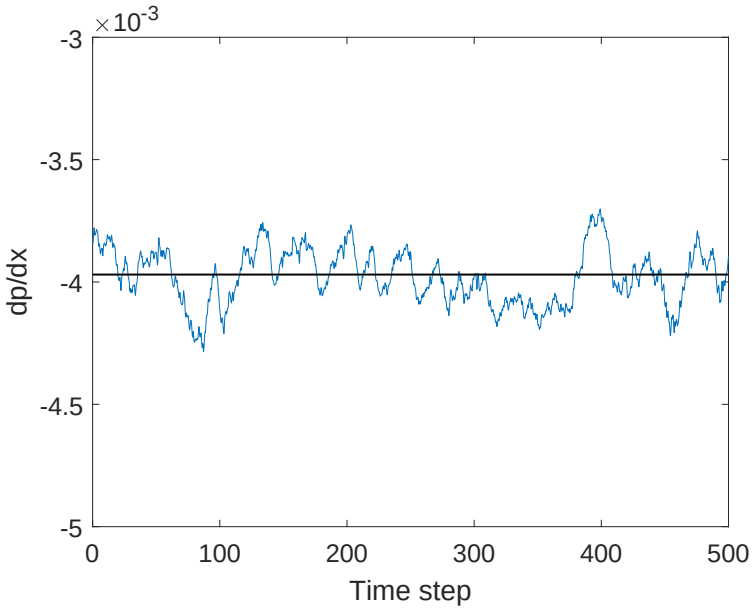

Figure 3.9: Pressure gradient time history for the channel with the smooth plates.

Therefore, going on with the timestep the pressure gradient oscillate in order to pursue the aforementioned condition. Figures 3.9, 3.10 and 3.11 show the fluctuation of the pressure gradient depending on the time. In order to obtain the drag reduction for each case, we need to compute the mean value of the pressure gradient; in fact, it is related to the drag performed from the two plates on the flow. The drag reduction for each case has been computed as follow,

$$DR = \frac{\overline{\frac{\partial p}{\partial x}}\Big|_0 - \overline{\frac{\partial p}{\partial x}}\Big|_i}{\overline{\frac{\partial p}{\partial x}}\Big|_0} \text{x}100, \tag{3.19}$$

where the subscripts 0 refers to the validation case, and the subscripts i indicates the case under consideration. Data reported in table 3.2 reveal that the simple triangular riblet surfaces produce a noticeable drag reduction respect to the smooth plates. Moreover, as expected from the value of Δh, the fractal riblet generate an even higher drag reduction. It seems reasonable the hypothesis of Luchini that an higher Δh produces an higher drag reduction. We recall that the drag reduction is obtained from the slip condition on the stream-wise velocity, that give the mean velocity profiles sketched in figure 3.12 and figure 3.13. It is clear in figure 3.12 and figure 3.13, that the stream-wise slip boundary condition affects the mean velocity profile as expected, in particular

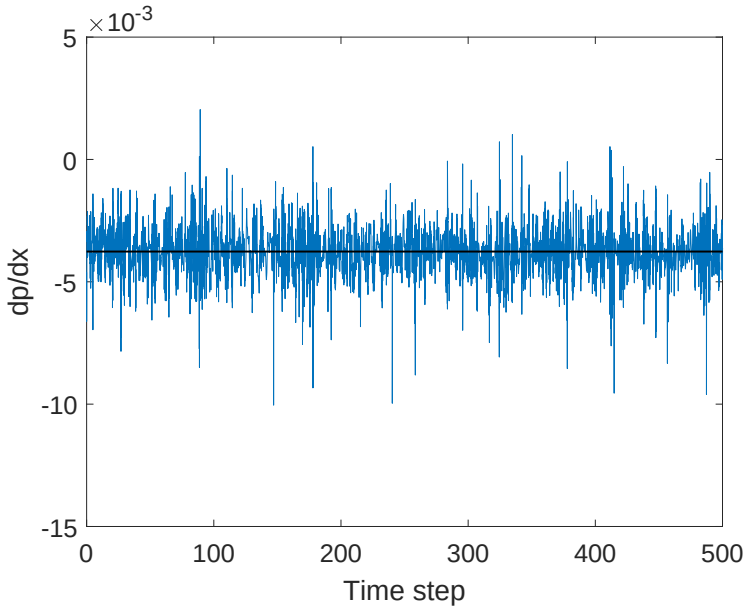

Figure 3.10: Pressure gradient time history for the channel with the 90° triangular riblet plate.

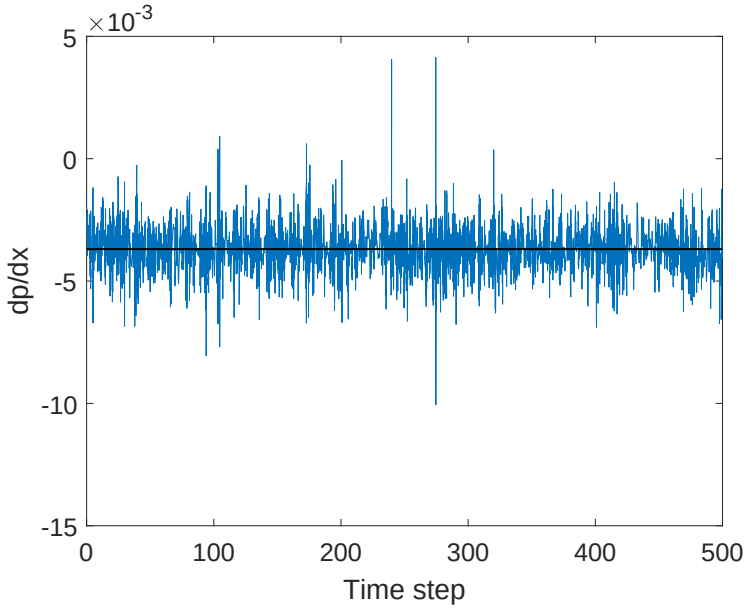

Figure 3.11: Pressure gradient time history for the channel with the third fractal iteratio 90° triangular riblet plate.

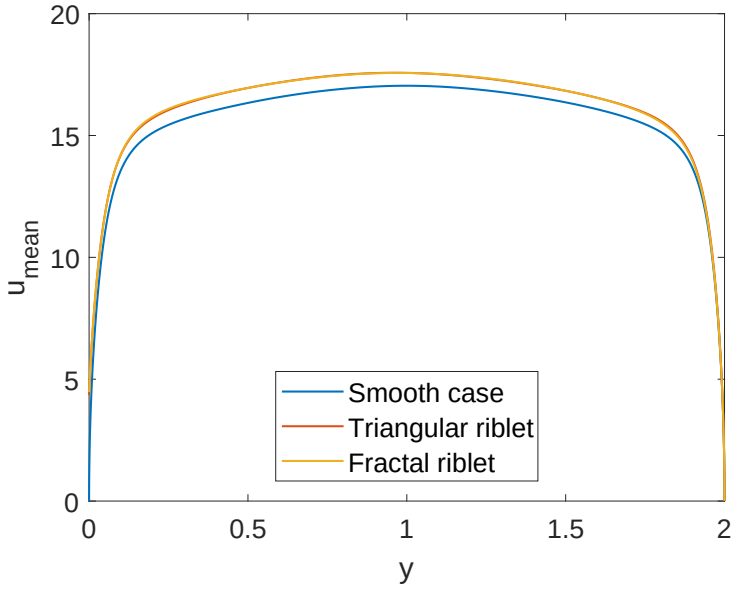

Figure 3.12: Mean stream-wise velocity profiles.

they are upward shifted. All the ribletted surfaces alter the logarithmic law as

$$u^+ = \frac{1}{k} log y^+ + C + \Delta U^+, \tag{3.20}$$

where $k \approx 0.41$ is the von Kármán constant and $C \approx 5.2$ and ΔU^+ characterizes the shift of the logarithmic region. A positive shift corresponds to drag reduction, whereas a negative shift corresponds to a drag increase, as on standard rough surfaces. This velocity shift is the key parameter to characterize riblet effects (Aupoix [2]), and the boundary condition adopted are able to reproduce it. Looking at figure 3.13 it is possible to note that the profile of the riblet cases are not only upward shifted, in fact the logarithmic zones of the profiles are nearer to the validation case then the near the wall profile. As carried out by T. Min and J. Kim [24], the pure stream-wise slip condition reveals a perfectly upward shifted mean velocity profile, whereas from the pure span-wise slip condition affect the logarithmic region with a downward shift. Eventually, when both the slip conditions are applied, a combination of behavior arise, as we have obtained in figure 3.13. The upward shift is noticeable between the smooth channel and the riblet channels, whereas it is almost zero between the fractal and the simple riblet channel.

The quantity that really contribute to the drag reduction is the gradient of the

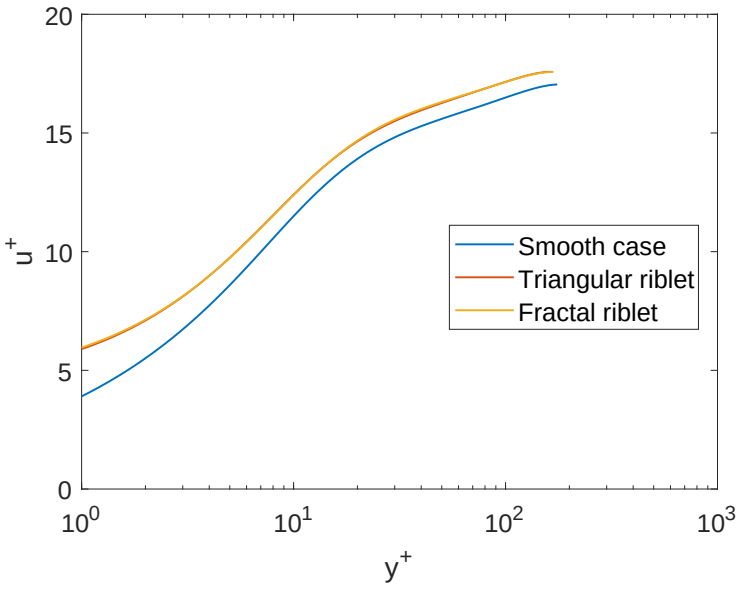

Figure 3.13: Mean stream-wise velocity profiles plotted on the y^+ coordinate (express in wall units) in semi-logaritmic scale.

velocity in the y direction, in fact it is related to the skin friction by well known relation 3.21

$$\tau_{wall} = \rho\nu \left.\frac{\partial \overline{u}}{\partial y}\right|_{wall} + \rho\overline{u'v'}, \tag{3.21}$$

where $\partial\overline{u}/\partial y$ represent the mean profile slope at the wall. As sketched in figure 3.14 fractal riblet shows the lower slope. Again the difference between the two riblet channel is quite small, and it cannot alone justify the drag reduction obtained with tha fractal riblet, therefore it is important looking at the turbulent effect. The skin friction is directly related to the shear velocity,

$$\frac{\tau_{wall}}{\rho} = u_\tau^2, \tag{3.22}$$

which decrease in the same way. The shear velocity trend is shown in figure 3.15 and figure 3.16. The root mean square of the istantaneous velocities are presented in figure 3.17, figure 3.18 and figure 3.19. The figures present the values of the root mean square on only the one half of the channel with the riblets wall, in fact the other half remain almost unchanged. The stream-wise component, presented in figure 3.17, show that each different case reach the maximum of the root mean square at the same y coordinate, however, in both the simple riblet and fractal case, the maximum has

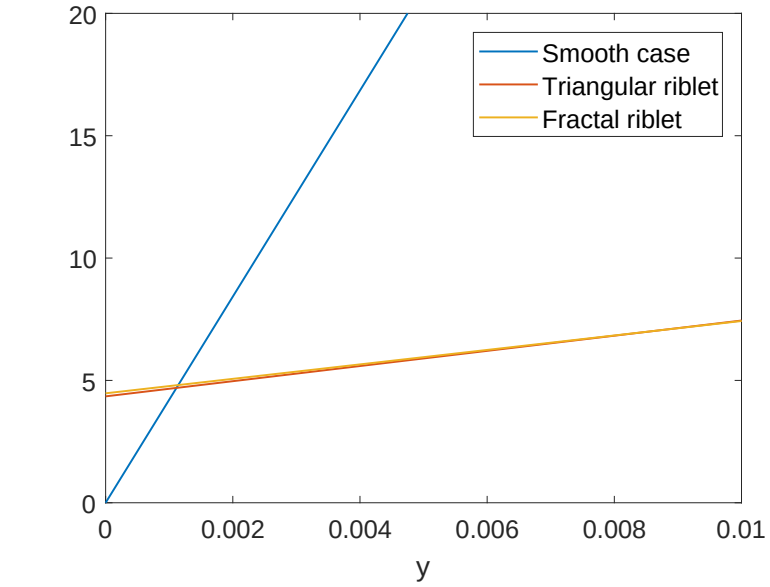

Figure 3.14: Near wall tangents to the mean stream-wise velocity profiles.

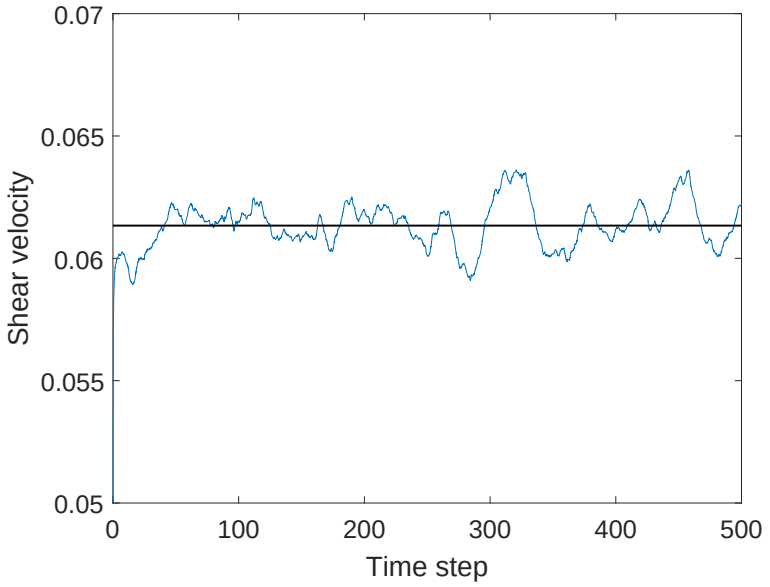

Figure 3.15: u_τ time history for the simple 90° triangular riblet.

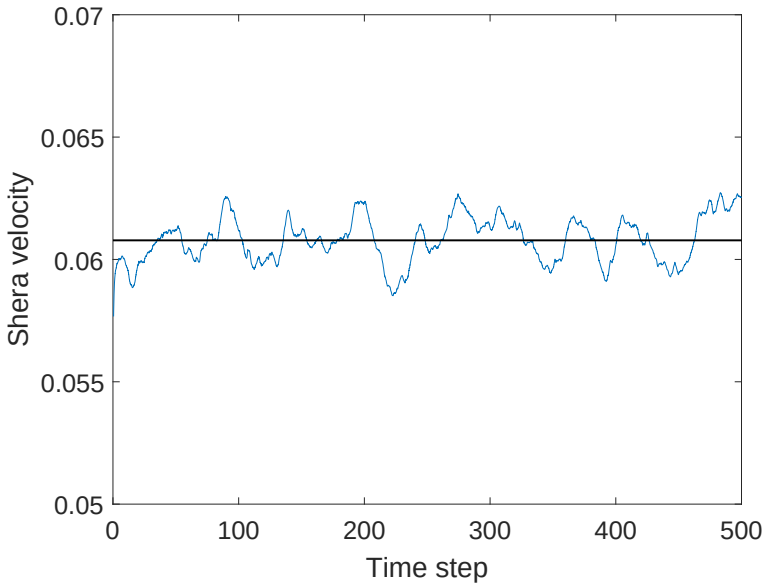

Figure 3.16: u_τ time history for the third fractalization for the 90° triangular riblet.

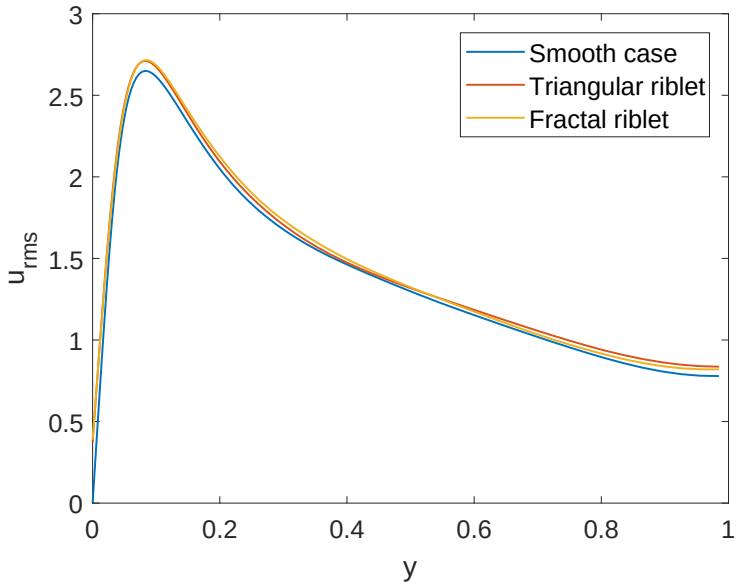

Figure 3.17: Root mean square of the stream-wise velocity. Each case is normalized by the actual value of u_τ.

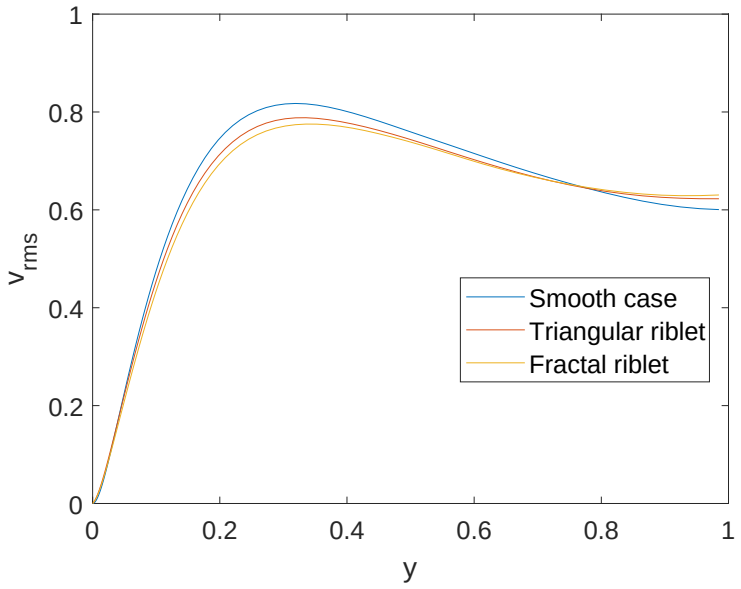

Figure 3.18: Root mean square of the normal velocity. Each case is normalized by the actual value of u_τ.

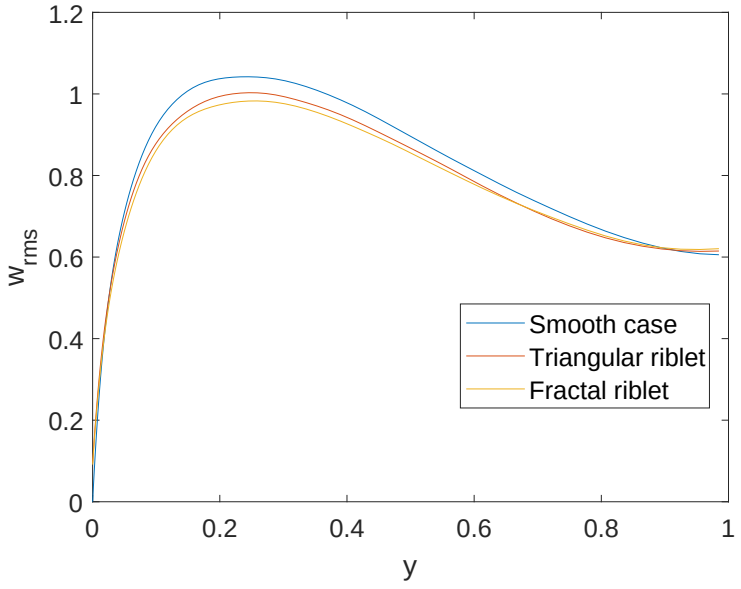

Figure 3.19: Root mean square of the span-wise velocity. Each case is normalized by the actual value of u_τ.

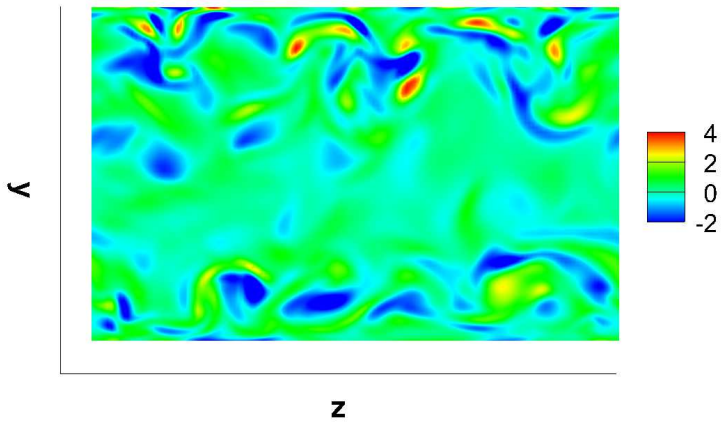

Figure 3.20: Contour of the stream-wise vorticity in the $z - y$ plane for the simple riblet channel.

an higher value. It is possible to argue that the Navier boundary condition generate an increment of the turbulent intensity of the stream-wise components of the velocity. This seems to be in contrast with the drag reduction, however if we look at the figure 3.18 and figure 3.19 we can figure out the problem. It is possible to note (in both the figure) that the three curves of the root mean square of the span-wise velocities coincide near the wall, but at certain y coordinates the simple riblet root mean square grow up slowly then the smooth case, and the root mean square of the fractal riblet grow up even more slowly then the simple triangular riblet. The velocities components plotted in figure 3.18 and 3.19 are responsible of the stream-wise vortex, therefore a reduction of both the root mean square indicates a dumping of the cross flow. The rms features reveal that the slip condition are able to reproduce the riblet effect, which works through the reduction of the cross-flow.

The reduction of the turbulence level can be confirmed by the values of the stream-wise and the span-wise vorticity. In figure 3.20 is presented the contour of the stream-wise vorticity in the $z - y$ plane; the bottom side of the channel present the grooved surface (here is applied the slip condition), and the top side the smooth wall (here is applide the no-slip condition). It is possible to note that near the no-slip wall are located a lot of spots of high vorticity, whereas the riblet surfaces show a lower generation of turbulence spots and the magnitude of vorticity is smaller. The behavior is due to the reduction of the bursting cycle.. Figure 3.20 confirms that the turbulent intensity is reduced by the riblet wall. In figure 3.21 it is possible to observe the span-

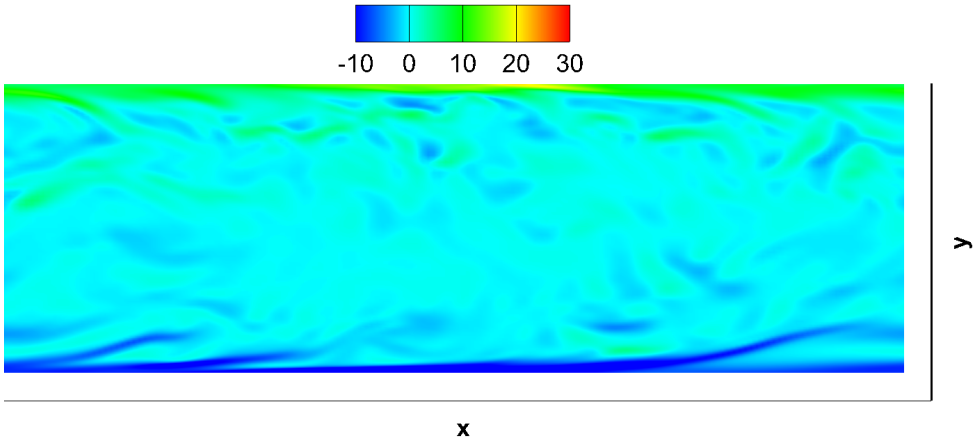

Figure 3.21: Contour of the span-wise vorticity in the $x-y$ plane for the simple riblet channel.

wise vorticity in the $x-y$ plane; again, the lower wall presents the riblet and the upper one is smooth. It is clear that in the upper zone of the channel an higher distribution of vortex is present. This effect can be related to the generation of vortices in the near wall region.

In order to asses the effect of the reynolds number, the DNS has been performed at $Re = 2200$ and $Re = 3500$. The results obtained are presented in table 3.3 and shown in figure 3.22.

Case	Re	$\lvert\partial p/\partial x\rvert$	u_τ	Re_τ
Smooth	2200	0.00395	0.0628	142
Smooth	2800	0.00397	0.0634	177
Smooth	3500	0.00370	0.0607	217
Riblet	2200	0.00385	0.0621	141
Riblet	2800	0.00376	0.0631	170
Riblet	3500	0.00351	0.0652	232

Table 3.3: DNS results for the smooth geometry and the 90° triangular riblet at different reynolds number.

It is possible to note the linear trend for both the smooth and the riblet plates, which

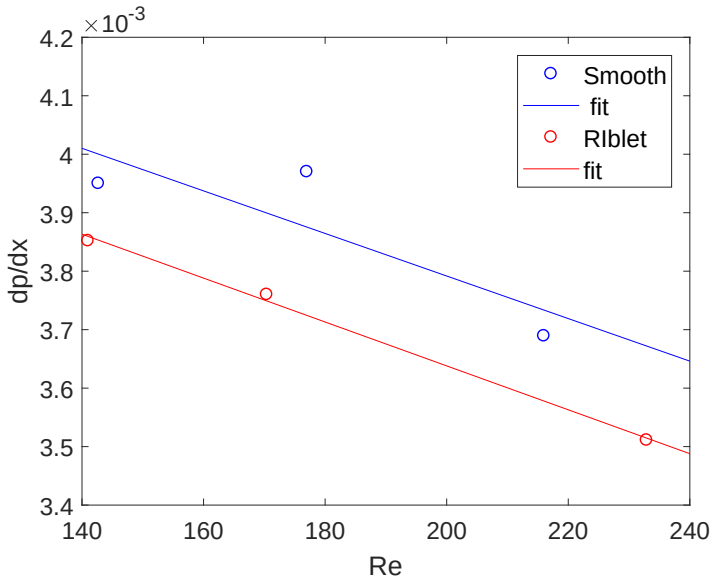

Figure 3.22: Pressure gradient at different reynolds number.

indicate a reduction of the drag when the Reynolds number increase. The riblet plates results shifted down, and this confirm that it is possible to obtain a drag reduction for each reynolds number herein considered.

Chapter 4

Conclusion

4.1 Conclusion

In this work we have studied, through numerical simulations, the drag reduction potentiality of a series of riblet surfaces generated by the fractalization of two different triangular riblet molds. In order to perform such simulations, we have subdivided the study in two parts: the microscopic and the macroscopic problem.

The first problem has been studied through the boundary element method. It is well known because of its capability to solve equations inside complex domains. It is turned out to be extremely efficient for the study of a two dimensional fractal geometry. The time required for the simulations was of the order of minutes; the longest simulation has required a time of only five minutes.

The microscopic problem has been solved for the two triangular riblet and their fractalization, in order to carry out the parallel and the perpendicular protrusion heights for each shape. The aforementioned values revealed an exponential trend, and that all the protrusion heights approach a finite limit when the fractalization go on, in particular, after the third iteration the protrusion heights didn't change anymore. This is a meaningful goal because confirm that the riblet effect is not affected by the nanoscopic feature of the surface, therefore, the roughness of the surface can be neglected when it is too fine. Another interesting results has been obtained thanks to the comparison of two kind of fractalization, one that protrude the geometry inside the fluid domain, and the other that protrude it inside the wall. The inward fractalization generates an increment of the protrusion heights and the difference between them; instead the outward fractalization generates a reduction of all the aforementioned quantities. Although the inward and the outward fractalization are symmetric respect to the triangular mold, the protrusion heights variation magnitudes are not. This indicates that the flow over a triangular riblet plates is more affected by a disturbance that protrude into the fluid rather then one that protrude into the wall. Moreover, the inward fractalization generate an increase of the difference between the parallel and the protrusion heights, and it is possible to argue, in line with the Luchini's theory, that the inward fractal riblet generate an higher drag reduction then the simple triangular one.

The second part of this work concerned the macroscopic problem; it allowed us to complete the study of the riblet plates and carry out the drag reduction. The triangular

riblet with the highest Δh and its third fractal iteration have been solved through the direct numerical simulation. In order to avoid all the difficulties that arise from the complexity of the riblet plates, the span-wise and the stream-wise Navier boundary conditions have been used. The simulation revealed that the simple triangular riblet plates and the fractal riblet plates are affected respectively by a drag that is 5.3% and 6.8% smaller then the smooth plates. As expected from the literature the simple riblet plates have a drag reduction in the range of $4-7\%$; it is clear that it would be possible obtain a better drag reduction with the triangular riblet, however this work does not aim at optimizing the shape of the riblet, rather it aim at studying the effect of nano-features of the riblet surfaces. Therefore, the important achievement consists in the percent of drag reduction obtained for the fractal riblet, that is almost 2 percent points higher then that obtained for the simple riblet. This results seems to confirm the role of the protrusion heights: they can be used to predict the efficiency of a riblet surface. The last statement must be yet carefully evaluated, in fact there are not experimental data in support of the representation of the riblet through the slip conditions. However, the computation of the root mean square of the velocity components seems to reveal that the physical mechanism generated by the presence of the slip conditions is the same that allow riblet to works.

The study herein performed seems to confirm the role of the protrusion heights, and that the slip conditions are capable to represent the riblet surfaces. However, the study of Taegee Min and John Kim [18] carry out that tough the difference between the parallel and the perpendicular protrusion heights (more precisely the stream-wise slip length and the span-wise slip length) is equal to zero, it is even possible to obtain a drag reduction.

4.2 Future developements

In the last years the researchers have focused their attention on a new kind of surfaces, which allow an higher drag reduction then riblets: the *Super-Hydrophobic* surfaces (SH in the following). The mechanism by which such a surface operate is completely different by the riblet one, and it is based on the high capability in repel water. This particular feature is due to the nano-structures present on the surface, that allow the surface to remain in the unwetted state, so that the fluid flow over the trapped air. SH surfaces are present in nature, for example, the two-scale structure of the bird's feather (figure 4.1) which renders it exceptionally waterproof, with air trapped underneath the network of barbs and barbules.

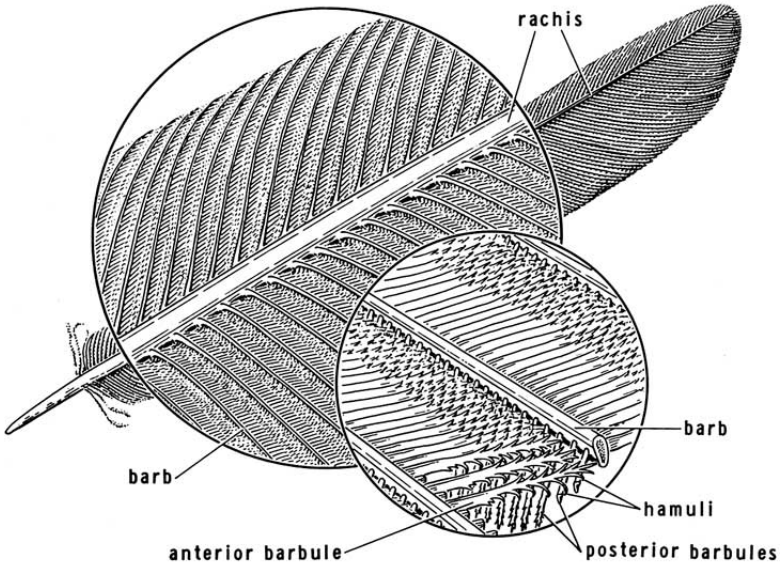

Figure 4.1: Bird's feather at microscope.

SH materials have received tremendous attention in recent years for the large variety of applications in which they could be put to profitable use, ranging from antiwetting to anti-icing, from self-cleaning to anti-corrosion, and obviously the drag reduction capabilities. Early experiments suggested that they reduce drag in both laminar and turbulent boundary layer flows. The SH surfaces are studied by a lot of researchers for the application in the naval field, in which a drag reduction up to 40% is possible.

The major problem with the SH surfaces concern the transition from the unwetted state to the wetted one, in which the drag reduction is compromised. This phenomenon is due to the dispersion of the air in the upper fluid. Nowadays, the principal solution

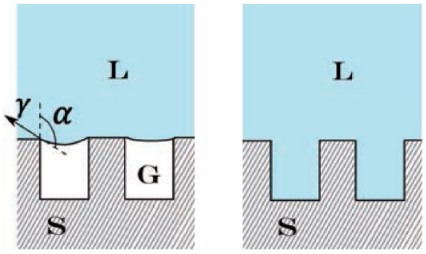

Figure 4.2: Unwetted state on the left and wetted state on the right.

consists in generating a fractal-like nano-structured surfaces, so that the air is trapped and the transition become slower.

The combination between materials and nano-technologies represent one of the most important field of study. It allows the construction of complex surfaces which are able to reduce the drag and contribute to the global energy saving.

Bibliography

[1] M. Quadrio A. Baron and L. Vigevano. On the boundary layer/riblets interaction mechanisms and the prediction of turbulent drag reduction. *Dipartimento di Ingegneria Aerospaziale del Politecnico di Milano, Milano, Italy*, 1993.

[2] R. Houdeville B. Aupoix, G. Pailhas. Towards a general strategy to model riblet effects. 2012.

[3] Burdak. Function of the ctenoid apparatus of fish in the presence of a turbulent boundary layer. *Journal of Fluid Mechanics*, 1991.

[4] Zayets Chernyshov. Some peculiarities of the structure of the skin of sharks. *Hydrodynamic Problems of Bionics*, 1970.

[5] Choi. Test of drag reducing riblets on a one-third scale racing yacht. *R. Aero. Soc. London*, 1987.

[6] A.j. Chorin. Numerical solution of the navier-stokes equations. 1968.

[7] Marc-Olivier Coppens. Characterization of fractal surface roughness and its infuence on diffusion and reaction. 2001.

[8] Jerry Henfer Dennis Bushnell. *Viscous drag reduction in boundary layers.* 1990.

[9] George Em Karniadakis Douglas C. Chu. A direct numerical simulation of laminar and turbulent flow over riblet-mounted surfaces. 1993.

[10] Youngs R. Wallace J.M. Hooshmand, D. An experimental study of changes in the structure of a turbulent boundary layer due to surface geometry changes. *AIAA*, 1983.

[11] P. Moin J. Kim. Application of a fractional-step method to incompressible navier-stokes equations. 1985.

[12] R. Moser J. Kim, P. Moin. Turbulence statistics in fully developed channel flow at low reynolds number. 1986.

[13] Parviz Moin Javier Jimenezi. The minimal flow unit in near-wall turbulence. 1990.

[14] Hsu S.-T. Liu J.-T. Kennedy, J.F. Turbulent flows past boundaries with small streamwise fins. *Journal of the Hydraulics Division*, 1973.

[15] P. S. Klebanoff. Characteristics of turbulence in a boundary layer with zero pressur gradient. *NACA TN-1247*, 1953.

[16] Daniel D.Joseph Luigi Preziosi, Kangping Chen. Lubricated pipelining. stability of core-annular flow. *Zool. Zh*, 1969.

[17] McLean. Flight-test of turbulent skinfriction reduction by riblets. *R. Aero. Soc. London*, 1987.

[18] Taegee Min and John Kim. Effects of hydrophobic surface on skin-friction drag. 2004.

[19] H. K. Moffatt. Viscous and resistive eddies near a sharp corner. 2012.

[20] Amilcare Pozzi Paolo Luchini, Fernando Manzo. Resistance of a grooved surface to parallel flow and cross-flow. *Journal of Fluid Mechanics*, 1991.

[21] Dinkelaker Reif. Hydrodynamics of squamation in fast swimming sharks. *Neues Jahrbuch fuer Geologie und Palaeontologie*, 1982.

[22] Javier Jiménez Ricardo García-Mayoral. Drag reduction by riblets. 2011.

[23] Winter Sawyer. An investigation of the effect on turbulent skin friction of surfaces with streamwise grooves. *R. Aero. Soc. London*, 1987.

[24] J. Kim T. Min. Effects of hydrophobic surface on skin-friction drag. 2004.

[25] Michael J. Walsh. Riblets as viscous drag reduction technique. 1983.

[26] G.Hoppe W.Bechert. On the drag reduction of the shark skin. 1985.

[27] M.Bartenwerfer W.Bechert. The viscous flow on surfaces with longitudinal ribs. 1988.

[28] Mario Zambini. Il peso del settore dei trasporti sui cmbiamenti climatici e le prospettive di contenimento delle emissioni. gli scenari internazionale ed europei. 2016.